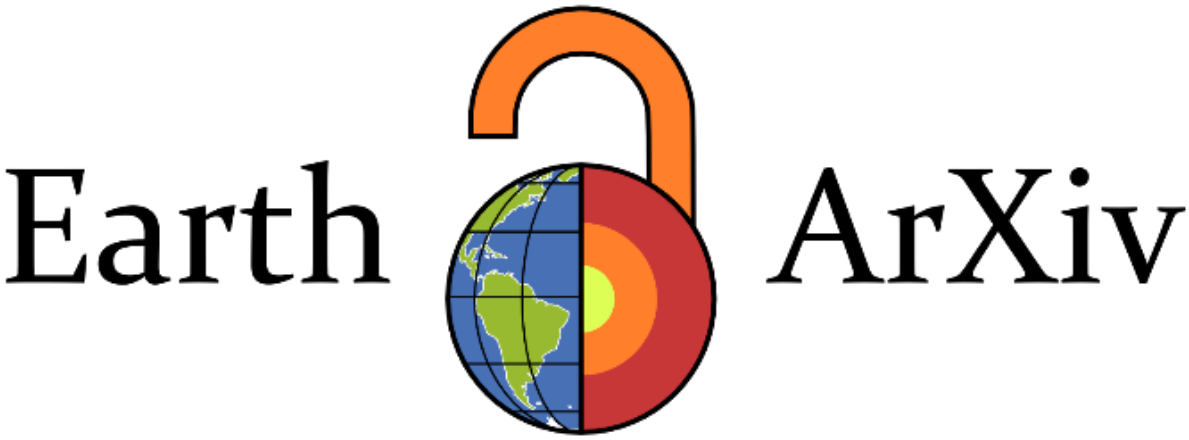


Peer review status:

This is a non-peer-reviewed preprint submitted to EarthArXiv.

How Greenland melts under cloudy and clear skies

Michael R. Gallagher[1,2,3]; Matthew D. Shupe[1,2,3]; Von P. Walden[4]; Anne Sledd[1,2,3]; Christopher J. Cox[2]; Heather Guy[5,6]; Claire Pettersen[7]; Andrew S. Martin[5,6]; Ryan R. Neely III[5,6]; Robert L. Hawley[8]; Michael S. Town[9]; Erik Olson[10]; Hans-Peter Marshall[11]; Derek Pickell[8]; Baptiste Vandecrux[12]; Laura D. Riihimaki[1,2,13]; Ruth Mottram[14]; Kyle S. Mattingly[10]; Laura Wilson[8]; David Clemens-Sewall[15]; Catherine Hebson[4]

[1]Cooperative Institute for Research in Environmental Sciences (CIRES), University of Colorado Boulder, Boulder, CO, USA; [2]NOAA Physical Sciences Laboratory (PSL), Boulder, CO, USA; [3]National Snow and Ice Data Center (NSIDC), University of Colorado Boulder, Boulder, CO, USA; [4]Department of Civil and Environmental Engineering, Washington State University, Pullman, WA, USA; [5]School of Earth, Environment and Sustainability, University of Leeds, Leeds, UK; [6]National Centre for Atmospheric Science (NCAS), Leeds, UK; [7]Department of Climate and Space Sciences and Engineering, University of Michigan, Ann Arbor, MI, USA; [8]Department of Earth Sciences, Dartmouth College, Hanover, NH, USA; [9]Earth and Space Research, Seattle, WA, USA; [10]Space Science and Engineering Center (SSEC), University of Wisconsin-Madison, Madison, WI, USA; [11]Department of Geosciences, Boise State University, Boise, ID, USA; [12]Geological Survey of Denmark and Greenland (GEUS), Copenhagen, Denmark; [13]NOAA Global Monitoring Laboratory (GML), Boulder, CO, USA; [14]Danish Meteorological Institute (DMI), Copenhagen, Denmark; [15]Institute for Arctic and Alpine Research (INSTAAR), University of Colorado Boulder, Boulder, CO, USA

Abstract

Greenland ice loss has risen sharply since industrialization[1] and will likely contribute 20 cm to sea level rise before 2100[2]. On the highest emissions pathway the ice sheet could melt by the year 3000, submerging coasts by 7.2 meters[3]. Greenland surface melt now dominates cryospheric mass loss[4,5]. To constrain the driving processes of this melt[6], here we present high-fidelity surface observations of clouds, energy, and melt on the lower southwestern Greenland ice sheet from summer 2024. Contrasting cloudy and clear (cloud-free) conditions, we find that firn energy storage primarily increases under

clouds, driven by the cloudy state's effect on surface radiation. Frequent optically thin clouds (LWP < 30 g·m^{-2}, 55% of observations) result in 26.5 W·m^{-2} more absorbed radiation at the surface than clear conditions on average. Near solar noon, when melt is most likely, peak absorbed radiation is 80% larger under cloudy skies (63 W·m^{-2}) than under clear (35 W·m^{-2}). A co-located automatic weather station underestimates the daily mean cloud effect by 30% and overestimates the peak clear-sky flux by a factor of two at solar noon, with implications for interpreting the in situ record that anchors Greenland's surface energy budget.

Main text

A complex set of melt processes at differing temporal and spatial scales makes the Greenland ice sheet the single largest mass contributor to sea level rise[7]. Therefore, to make informative and skillful projections of future mass loss, models must accurately emulate the full range of processes that modify the surface energy budget and melt. Moreover, assessing the accuracy of those projections requires observations of parameters that models struggle to represent. Recent studies have found that the primary uncertainties in model projections of Greenland surface mass loss are cloud microphysics[6] and the spatio-temporal evolution of albedo[8,9]. These uncertainties are further enhanced by feedbacks involving surface melt, firn pack, precipitation processes, and atmospheric properties[10], all of which are poorly constrained by observations.

The size, relatively low latitude, and geography of the largest ice sheet in the Northern Hemisphere are a prime setting for rapid change. Southern Greenland, positioned at the confluence of the North Atlantic storm track and Gulf Stream, is

uniquely sensitive to heat transport into the Arctic[11]. Thus, this region serves as an early indicator of Arctic-wide warming trends with possible connections to severe climatic feedbacks[12,13]. As Greenland has warmed over past decades, the total area susceptible to surface melt has increased[14,15] and the summer snowline has migrated to higher elevations with increasing variability[16,17]. All these factors lead to an increased sensitivity of the surface to cloud cover and its synergistic relationship with firn properties, such as albedo and refreezing of surface melt as they vary with elevation[18].

Changing Greenland melt

Nowhere is it more important to observe these processes than the southwestern Greenland ice sheet, where runoff area is increasing more rapidly than any other region[19] as the ice sheet's mass equilibrium has destabilized[20,21]. Southwestern Greenland has also seen a major shift in spatial melt extent. The mean 30-day melt line, the contour enclosing areas experiencing ≥30 melt days per year, has moved ~50 km up the ice sheet in the past three decades (Fig. 1).

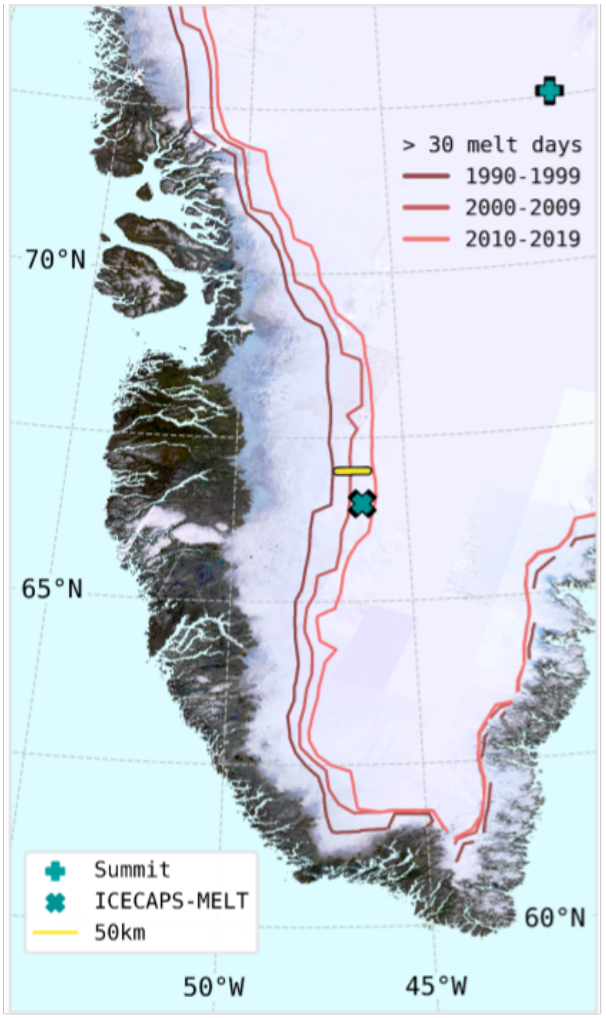


Fig. 1 | Decadal changes in mean 30-day melt line of the Greenland ice sheet from observations of melt occurrences in the NASA MEaSUREs dataset[23]. Underlying image stitched from visible spectrum Landsat data on July 5th 2016 shows approximate mean position of important ice sheet surface features. Summer 2024 "MELT" observational campaign shown by the "x" with ICECAPS Summit research station as the "+" symbol.

As melt reaches higher elevations, it will drive dynamic changes in the physical processes that influence mass balance and surface melt itself. To observe the interplay of these critical physical processes at this nexus of warming, the Integrated Characterization of Energy, Clouds, Atmospheric state, and Precipitation at Summit (ICECAPS) program expanded from its 15-years of measurements at Summit Station[22] to make observations in the rapidly changing percolation zone. Our team deployed a novel research platform to collect high-fidelity observations of melt-related properties and their interconnected processes in summer 2024 near the DYE-2 site on the southwestern Greenland ice sheet at 2094 meters elevation and 140 km from the ice edge (Fig. 1). Because the percolation zone is expected to expand significantly with warming, this site serves as a bellwether since the physical drivers of melt observed here today offer a critical preview of how the ice sheet interior will likely evolve in the future.

Operating a combination of key instrumentation autonomously, from microwave radiometry of the atmosphere to ground-penetrating radar of the firn, enables new insights on the coupled atmosphere-ice interactions that drive Greenland melt processes and hinder climate projections. Together, these observations can provide insight into a range of existing hypotheses relating to melt, from preconditioning of the ice sheet energy balance[24], to the mechanistic influence of clouds on refreezing of percolating meltwater[25], to the freshening of albedo by snowfall[26], and more. The team designed, engineered, and built a sophisticated platform to usher in a new autonomous, cross-cutting observational capability for quantifying the complex surface processes happening within the rapidly expanding domain of Greenland melt.

From the resulting data, we juxtapose observations of cloudy and clear-sky melt days on the lower ice sheet to clarify details of the cloudy-clear dichotomy often presented in the melt literature[27,28]. Our understanding of these mechanisms remains incomplete, with recent studies yielding divergent interpretations of how clouds modify the surface energy budget[29]. We focus on this dichotomy because recent studies highlight cloud microphysics as a dominant uncertainty in future mass loss projections[6,10] and observational constraints on the complex interplay of cloudy atmospheric states in the rapidly expanding melt zone remain sparse[30]. First, the atmosphere, upper firn, and influential coupled processes are examined for individual cloudy and clear-sky melt events observed during summer 2024 to contrast these two melt pathways. Then, differences between the cloudy and clear-sky atmospheric states are quantitatively evaluated from two perspectives: an aggregate diurnal schema that shows the evolution of cloudy and clear-sky days, and a probabilistic framework that relates the full range of cloud characteristics to their influence on the surface radiative energy budget. Independent firn temperature observations are then used to test whether the radiative state differences observed at the surface map coherently onto changes in the energy content of the upper 20 cm of firn. Together, these perspectives construct a comprehensive picture of how cloudy conditions affect the surface of the melting Greenland ice sheet. For broader ice sheet context, a comparison to co-located automatic weather station (AWS) data is included, since these are the only in situ measurements available for evaluating surface processes and melt drivers at many locations across the ice sheet.

New observations of the ice-air interface

More than 20 instruments with 100+ sensors were deployed as components of the autonomous science platform, with data transmitted for analysis in near real-time. From these data, Figs. 2 and 3 show illustrative contrasting cloudy and clear-sky melt events. Here, the focus is on observations of clouds, radiation, and melt processes. A comprehensive treatment analyzing the complexities of turbulent fluxes, conductive heat transfer, meltwater refreeze, and energy budget closure will be addressed in forthcoming work.

During the summer 2024 measurement period, we observed 15 days with considerable surface melt (Methods: Identifying melt; Extended Data Figs. 8 and 10). These melt days occurred across 6 distinct events with intervening periods of refreeze. Four events featured predominantly cloudy conditions, while two were mostly clear. Although there are many compelling features from each event, we first focus on two exemplary yet contrasting melt events (Figs. 2 and 3) to demonstrate distinct features of the coupled atmosphere-ice evolution under cloudy and clear-sky conditions. Then the full summer is analyzed to provide context and quantify crucial cloud and energy processes. Measurements range from cloud properties (Figs. 2 & 3, a,b,c), through specialized surface broadband radiation sensors[31] (Fig. 2d), to the firn characteristics they impact (Figs. 2 & 3, e,f,g). The clear-sky melt event (Fig. 2) occurred shortly after the initial transition into the summer melt season on June 16, while the cloudy melt event occurred on June 28 (Fig. 3). Because energetic accumulation and firn hysteresis

influence melt evolution during individual events, Figs. 2 and 3 also include the 3 days preceding melt.

Energetic mechanisms of cloudy and clear-sky melt

From 13:00 to 20:00 (all times are in UTC, solar noon at 15:00) on June 16, surface melt (*Methods: Identifying melt*) was recorded by firn temperature sensors (Fig. 2g), the 5Ghz ground penetrating radar (GPR) attenuation derived melt index (Fig. 2i), and surface skin temperature derived from longwave radiation (Fig. 2f). This melt occurred near the end of a sustained five-day period of clear skies (Fig. 2a), from June 13 until early June 17. This event, featuring a remarkably extended clear-sky period, was punctuated at the end by surface melt at peak solar flux on June 16.

Near-surface air temperature (Fig. 2f) followed a pronounced diurnal cycle with daytime peaks (solar noon at 15:00) just above 0 °C and nighttime lows (23:30 to 05:30) below -10 °C. Shortwave absorption near solar noon briefly peaked near 150 $W \cdot m^{-2}$. In comparison, surface net longwave radiative losses approached -100 $W \cdot m^{-2}$ during the day and -50 $W \cdot m^{-2}$ at night (Fig. 2e). Sustained melt only occurred after three days of subsurface warming, demonstrating how persistent longwave losses in clear-sky conditions oppose melt and dominate the radiative budget except at peak solar input. For this clear-sky event, efficient radiative energetic losses from the surface layer during cloud-free nights must be overcome by daytime energy fluxes before melt can occur.

Subsurface heat fluxes (Fig. 2h) change with surface meltwater production, leading to increased energy transfer downward through the firn. The warm subsurface pulses lag the surface fluxes by approximately 12 to 24 hours from 50 to 100 cm in depth.

A notable feature of this period is the steady surface albedo decrease across the clear-sky days preceding melt (Fig. 2d). As snow is exposed to heat and sunlight, snow grains metamorphose and darken[32,33], reducing albedo and increasing absorbed solar energy, leading to melt. The rapid melt cessation also demonstrates the importance of albedo: on June 18, snowfall restored surface brightness, increasing albedo from 0.81 to 0.88 and reducing absorbed solar radiation by 37%. This surface change effectively quenched the melt despite the air temperature remaining near 0 °C. Surface snow accumulation over this period was 2 to 5 cm with some variation across the surface topography as measured by GNSS reflectometry (Fig. 2g; Methods: Snow accumulation and surface roughness).

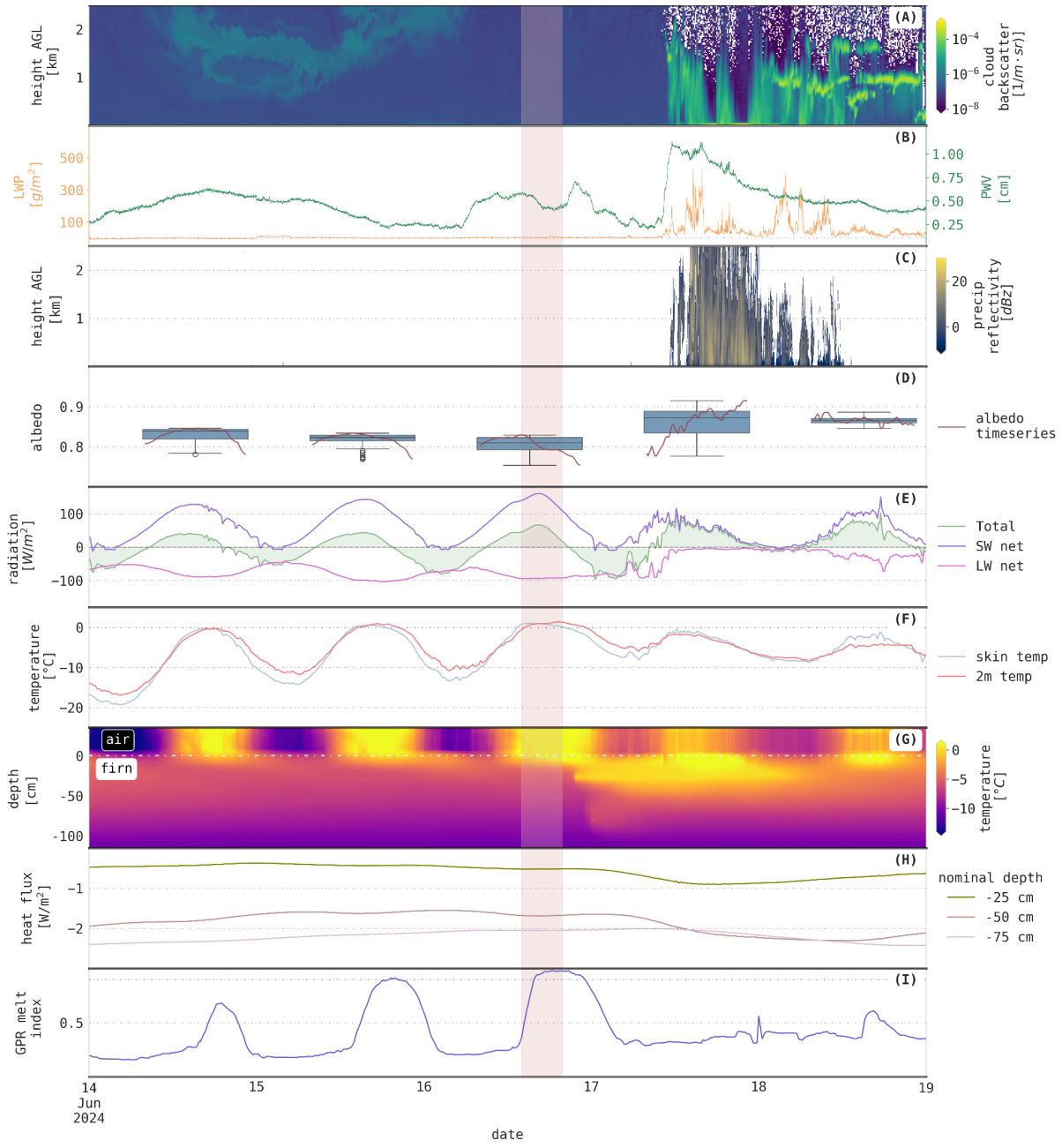


Fig. 2 | Clear, cloud-free, surface melt event on June 16. Melt is identified using a combined suite of sensors, and the melt time is highlighted in red. Panels from top to bottom organized from atmosphere down through observations: (a) lidar backscatter (b) atmospheric liquid water path and precipitable water vapor (c) precipitation radar reflectivity (d) surface albedo box (blue) and timeseries (red) (e) net radiative fluxes for longwave, shortwave, and total budget (f) skin and 2 m air temperatures (g) firn subsurface temperatures normalized to nominal surface height at installation (h) subsurface heat fluxes at depths with respect to nominal height (i) melt index from GPR 5Ghz signal attenuation.

From 12:00 to 21:00 on June 28, surface melt was recorded (Fig. 3f,g,i) amid an extensive 12-day period of mostly cloudy skies (Fig. 3a; Extended Data Fig. 10a). Consistent snowfall during this cloudy period led to the largest accumulation of the summer, with precipitation before, during, and after the melt. In the days around the melt event, 10-15 cm of snow accumulated on the ice sheet surface (Fig. 3g; Methods: Snow accumulation and surface roughness).

Over this time, albedo fluctuated with snow accumulation and melt. On June 27, the day before the melt occurred, precipitation raised the albedo to 0.90. During the sustained melt on June 28, albedo then decreased to 0.84 despite concurrent precipitation. Snowfall then continued through June 29, when renewed fresh accumulation again increased the albedo to 0.91.

During melt, the near-surface air temperature and retrieved surface skin temperature (Fig. 3f) were elevated to just above 0 °C. Meltwater production was sustained across a 9-hour period, as shown by the GPR melt index (Fig. 3i). Here, refreeze during the night following the melt event was strongly inhibited by cloud trapping of longwave radiation, and thus GPR attenuation caused by the presence of liquid water in firn was observed into the next day. This stands in stark contrast to the rapid refreeze of melt in the clear sky case (Fig. 2i) and provides a detailed in situ study of a case analogous to the results from Van Tricht et al. (2016)[27], with cloud at night inhibiting refreeze of the surface.

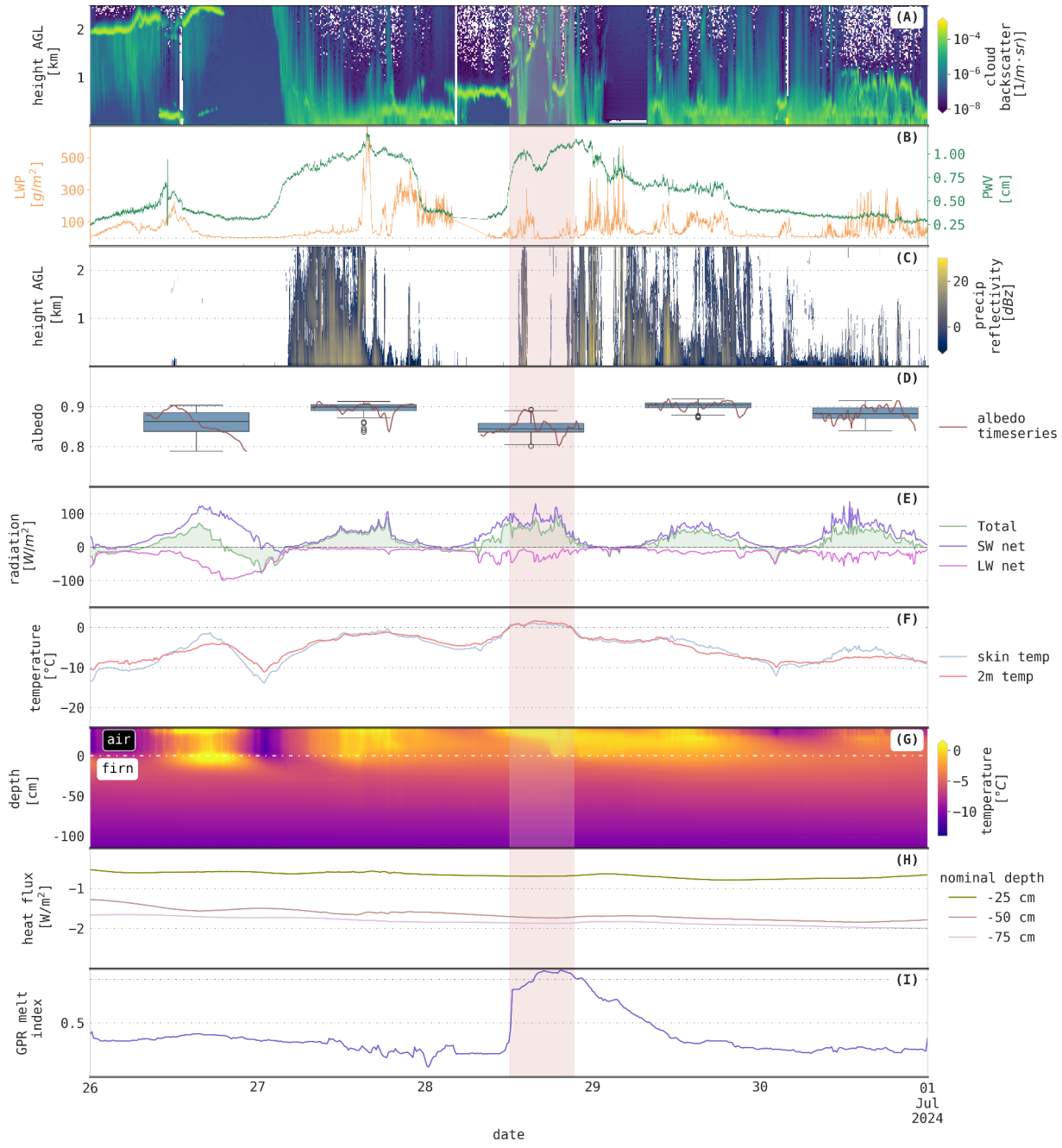


Fig. 3 | Cloudy conditions surface melt event study on June 28. Melt is identified using a combined suite of sensors, and the melt time is highlighted in red. Panels from top to bottom organized from atmosphere down through subsurface observations: (a) lidar backscatter (b) atmospheric liquid water path and precipitable water vapor (c) precipitation radar reflectivity (d) surface albedo box (blue) and timeseries (red) (e) net radiative fluxes for longwave, shortwave, and total budget (f) skin and 2 m air temperatures (g) firn subsurface temperatures normalized to nominal surface height at installation (h) subsurface heat fluxes at depths with respect to nominal height (i) melt index from GPR 5Ghz signal attenuation.

The cloudiest days of this event saw the lowest incoming shortwave flux of the entire observation record (Extended Data Fig. 10e), despite being near the summer solstice. However, the total radiation absorbed by the firn surface (Fig. 3e) during this melt period was larger than that during the melt day in the clear-sky case (Fig. 2e) due to additional surface longwave radiative warming. On June 16th, the clear-sky melt day, the surface absorbed 1.1 MJ·m^{-2} of radiation from 05:30-23:30, while during the same time frame under cloudy conditions on June 28, the surface absorbed 2.3 MJ·m^{-2}. The key difference was the nighttime radiative loss being near zero in the cloudy case compared to -70 W·m^{-2} in the clear-sky case.

To compare the energetic pathways that produce these contrasting outcomes, we examine the individual radiative components of the surface budget for cloudy and clear-sky days. The total radiation absorbed by the surface (eqs. 1) comprises net shortwave (incoming minus reflected) and net longwave (downward atmospheric emission minus surface emission) radiative fluxes. Processes that modify those individual fluxes therefore modify the total amount of radiative energy absorbed.

For either cloudy or clear sky cases, the total radiation absorbed by the surface, Q_{net}, is the sum of the net shortwave (incoming minus reflected) and net longwave (downward atmospheric emission minus surface emission) radiative fluxes:

$$Q^{s}_{net} = SW^{s}_{net} + LW^{s}_{net} \qquad 1a$$

$$SW^{s}_{net} = SW^{s}_{\downarrow} - SW^{s}_{\uparrow} \qquad 1b$$

234 $$LW^{S}_{net} = LW^{S}_{\downarrow} - LW^{S}_{\uparrow} \qquad 1c$$

235

236 Downwelling shortwave and longwave radiation are both modulated by clouds
237 through interdependent properties, including height above the surface, cloud
238 temperature, emissivity, and cloud composition (ice, supercooled droplets, or
239 mixed-phase). In comparison, the outgoing longwave and reflected shortwave are
240 dependent on surface properties like albedo, emissivity, and skin temperature. Aspects of
241 both incoming and reflected shortwave radiation depend on solar zenith angle (SZA).
242 While these interconnected processes occur across the planet, there are many unique
243 aspects in the Arctic[34]. In Greenland, clouds are often warmer than the surface due to
244 frequent temperature inversions, relatively optically thin, and frequently contain liquid
245 even at low temperatures[35,36]. Sophisticated cloud measurements are difficult to make on
246 the ice sheet, and liquid water path (LWP) has been identified as a first-order proxy for
247 cloud properties that modify the Arctic radiative budget[34]. There are crucial radiative
248 dependencies on Arctic cloud LWP for both downward longwave and shortwave fluxes
249 at the ice surface. While cloud longwave emission reaches saturation at LWP ≥30 $g \cdot m^{-2}$,
250 shortwave transmission continues to decrease at higher LWPs. Therefore, optically thin
251 clouds of 0-50 $g \cdot m^{-2}$ can have a large positive impact on the Arctic radiative budget, and
252 the radiative budget is particularly sensitive to LWP <30 $g \cdot m^{-2}$ depending on the cloud
253 properties outlined above[35].

254

Returning to these events, we can quantify the individual components driving the energetic differences described above to compare their radiative states. During the cloudy melt event (June 26th-29th), we observed a median LWP of 41 g·m $^{-2}$ (Methods: Measuring LWP) and a mean cloud base height of approximately 250 meters above ground level (Fig. 3a,b). At this LWP, the longwave trapping is near-maximized while shortwave attenuation is moderate, producing a strong net positive radiative flux. For these cloudy melt days, SW_{net}^{cloudy} = 3.7 MJ·m^{-2}, LW_{net}^{cloudy} = -1.4 MJ·m$^{-2,}$ and sum to Q_{net}^{cloudy} = 2.3 MJ·m^{-2}.

For the clear-sky case, these values were 6.5 MJ·m $^{-2}$ and -5.5 MJ·m^{-2}, a total of 1.1 MJ·m^{-2}. While these are aggregate values for these events, the surface radiative response to LWP variability is evident in the time series: brief cloud gaps (near-zero LWP) correspond to increased net longwave losses. At the same time, periods of higher LWP values are associated with reduced losses. Similarly, net surface shortwave absorption increases during cloud gaps. To generalize beyond these individual events, we now analyze the complete summer 2024 dataset, quantifying how cloud conditions relate to the full range of observed surface radiative states.

Cloudy and clear sky radiative states

Having established detailed mechanisms through which clouds affect the evolution of these melt cases, we now systematically quantify the differences between cloudy and clear states.

Following the generalized analysis of cloud impacts on Arctic sea ice presented in Shupe et al. (2026)[37], to quantify important differences in the cloudy and clear-sky states

over Greenland we define the atmospheric state effect of clouds on Q_{net} as the difference between the states of cloudy and clear conditions as:

$$E^{clouds}(Q_{net}) = Q_{net}^{cloudy} - Q_{net}^{clear} \quad (2)$$

By partitioning the summer of observations into cloudy and clear-sky atmospheric states, eq. 2 quantifies the differences between the integrated atmospheric conditions when clouds occur versus clear-sky conditions. Thus, $E^{clouds}(Q_{net})$ quantifies implicit observed differences in thermodynamic profiles, water vapor, near-surface stability, and more that accompany shifts in cloudiness. There are two values of the atmospheric state effect that can be calculated, the maximum effect as shown in Eq. 2 that is the difference between the average observed states. Or the difference scaled by the occurrence frequency of each observed state. Here, because we do not have enough atmospheric profiling data to report on climatological frequency of cloudy or clear conditions, we report only the observed mean difference between the two observed states.

This quantity is functionally equivalent to what has been termed "measurement-based" cloud radiative forcing (CRF) in recent cryospheric literature,[38,39] though the term CRF has been applied inconsistently across studies without rigorous distinction between fundamentally different methodologies. As Stapf et al. (2021)[39] demonstrated, a measurement-based approach comparing observed fluxes in different atmospheric states is distinct in interpretation from radiative transfer-based CRF values that subtract a modeled clear-sky reference from observed all-sky fluxes while preserving

the thermodynamic profile of the cloudy atmosphere[40,41]. These approaches answer different physical questions with differing availability of data. We adopt the atmospheric state effect notation to make the methodological distinction explicit. However, our reported values can be compared to measurement-based CRF estimates such as Wang et al. (2018)[42].

For calculating values from Eq. 2, we identify cloudy conditions using active cloud lidar that distinguishes overhead clouds by backscatter, validated with auxiliary information that is provided by a suite of sensors and cameras (*Methods: Cloud identification)*. Fig. 4 captures the evolution of individual components of Eq. 2 across the diurnal cycle of solar radiation to show how cloudy and clear states relate to longwave (4a), shortwave (4b), and total (4c) radiation at the ice sheet surface.

Averaging across the diurnal cycle yields the mean components of Eq. 2 to calculate the observed mean effect of a cloudy atmospheric state on radiation. In cloudy conditions, the daily mean net surface longwave flux was -24.3 $W \cdot m^{-2}$, the net shortwave flux was 40.9 $W \cdot m^{-2}$, and the combined total radiative flux Q_{cloudy} was 16.6 $W \cdot m^{-2}$. For clear conditions, the mean net longwave flux was -75.7 $W \cdot m^{-2}$, the net shortwave flux was 65.8 $W \cdot m^{-2}$, and the combined total radiative flux Q_{clear} was -9.9 $W \cdot m^{-2}$. From these components the atmospheric state effect of clouds on radiation $E^{clouds}(Q_{net})$ was 26.5 $W \cdot m^{-2}$, equating to 2.29 $MJ \cdot m^{-2} \cdot day^{-1}$ more radiative energy in cloudy conditions than clear on average. For context, 1 MJ is roughly enough energy to melt 3 kg of ice.

While $E^{clouds}(Q_{net})$ is a useful summary statistic, the complete diurnal cycle (Fig. 4) demonstrates critical features in the timing of radiative fluxes. Adequately characterizing

meltwater production requires capturing both the energetic evolution toward melt and fluxes during melt. The peak average radiative flux at solar noon (Fig. 4c) was 63 W·m $^{-2}$ for cloudy versus 35 W·m^{-2} for clear. This difference arises because frequent optically thin, low-LWP clouds enhance longwave radiation more than they attenuate shortwave radiation even at maximum solar irradiance. Consequently, not only is the mean $E^{clouds}($ Q_{net} $)$ 26.5 W·m^{-2}, but peak net radiative absorption is 1.8 times larger under optically thin clouds. These observations depart from model results in Van Tricht et al. (2016) [27], which suggested that clouds enhance radiation primarily through nighttime longwave trapping, compensating for daytime radiative deficits.

These findings contrast previous cloud process studies using in situ data from AWS in this region[30] in both the magnitude and diurnal character. So to assess this discrepancy, Fig. 4 includes observations from the DY2 AWS located 3 km northeast. DY2 is part of the Greenland Climate Network (GC-Net) operated by the Geological Survey of Denmark and Greenland (GEUS), which, with the Programme for the Monitoring of the Greenland

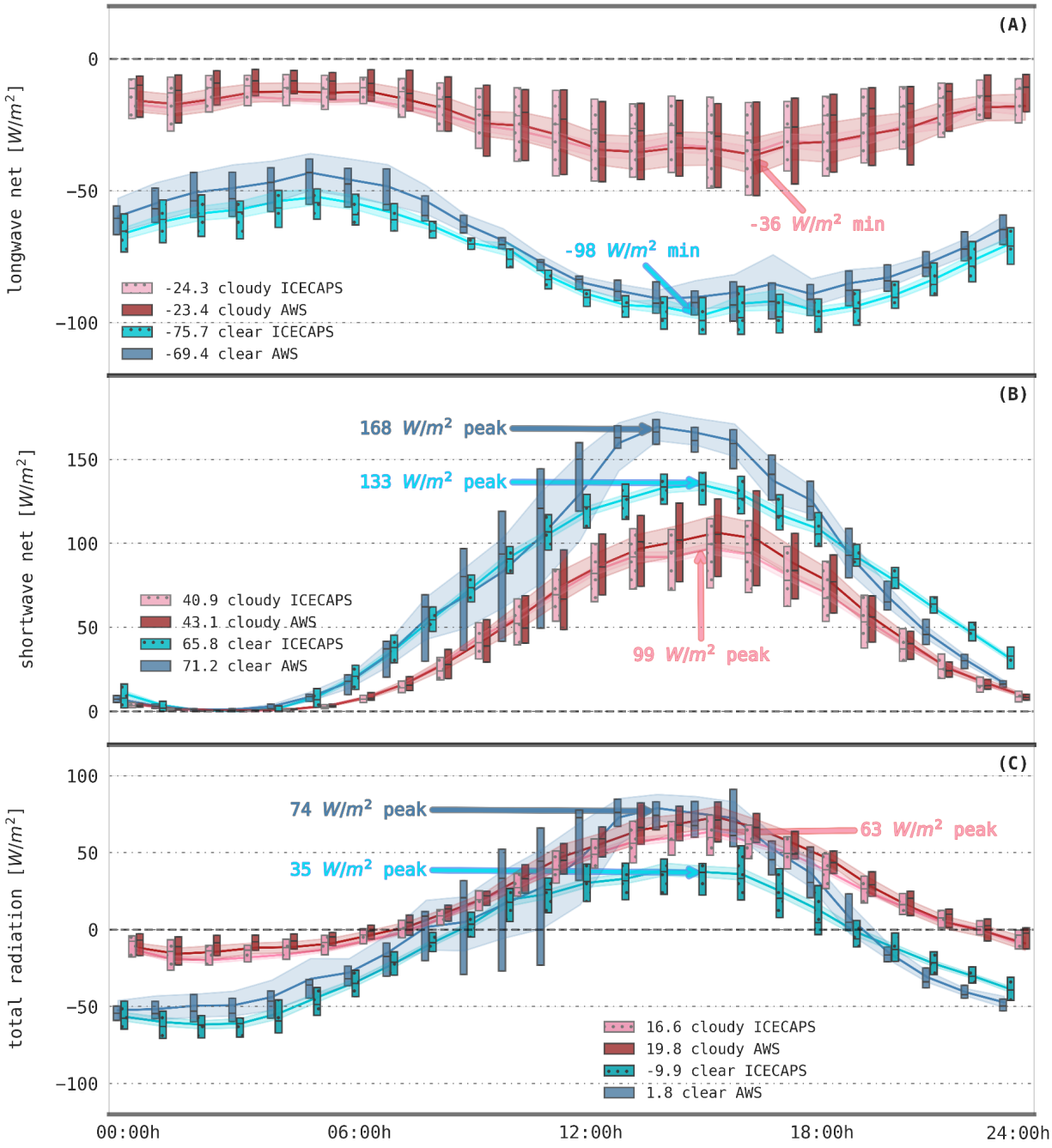


Fig. 4 | The aggregate radiative diurnal cycle for cloudy and clear-sky conditions observed during summer 2024 for radiation in (a) longwave, (b) shortwave, and (c) total radiative fluxes. Cloudy and clear-sky classification is determined by the integrated lidar backscatter (*Methods: Cloud identification*). Co-located AWS data are plotted in darker colors. Mean values for the entire observed period are shown in the legend.

Ice Sheet (PROMICE) network, are the main providers of year-round in situ observations of critical ice sheet surface variables[43]. Designed for robustness and deployability, GEUS AWS measurements operate on a strict power budget and with more basic instrumentation than the ICECAPS system.

AWS observations average $E^{clouds}(Q_{net})$=19.8 W·m^{-2}, about 75% of that measured by the ICECAPS sensors. This disparity is driven mostly by large differences in clear sky downwelling surface radiative fluxes that are only partially compensated by smaller differences in cloudy sky values. The net AWS fluxes under both cloudy and clear-sky conditions are larger than those from ICECAPS, but the differences in cloudy conditions are modest, with AWS slightly higher than ICECAPS for daytime net shortwave and nighttime net longwave radiative fluxes. The pattern emerges more strongly for clear sky conditions, which is typical of radiometric comparisons. The clear-sky AWS surface net longwave flux is about 6 W·m^{-2} larger throughout the day. Similarly, daily peak absorbed shortwave radiative flux is 26% larger for the AWS and the AWS clear-sky net shortwave flux shifts to being less than the ICECAPS value for the last four hours of the day. These shortwave differences are consistent with sensitivities in sensor response to varying incident angles of the low-elevation direct beam of the sun[44], which are expected to be larger in the upward-facing AWS pyranometer compared to the ICECAPS sensor, and in the AWS more than compensates for the concurrent differences in clear sky net longwave flux. Consequently, the AWS sensors measure a peak clear-sky net radiative flux (74 W·m^{-2}) that is more than twice as large as measured by ICECAPS (35 W·m^{-2}), suggesting that the radiative balance in cloudy and clear-sky conditions across the

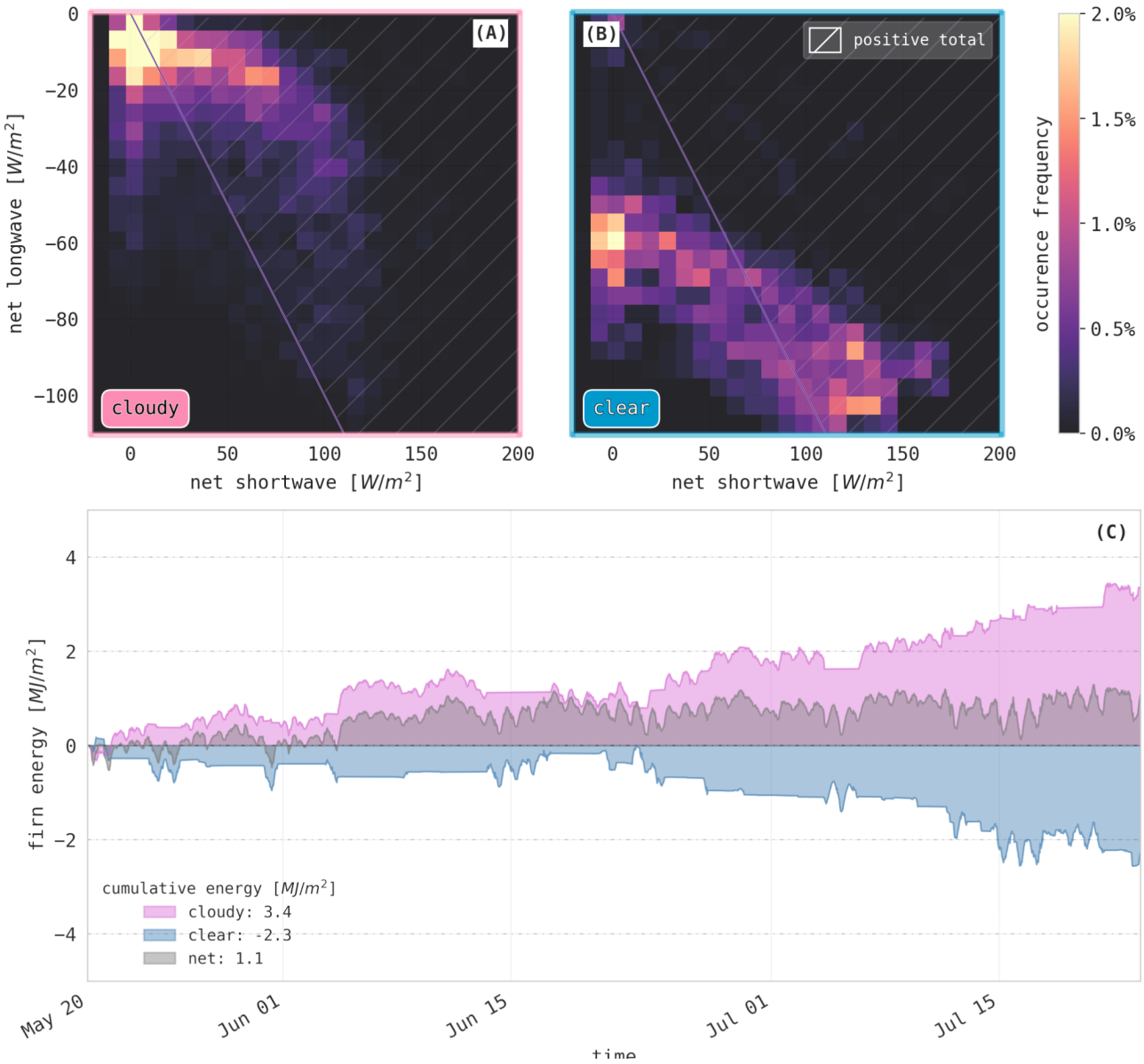
366 diurnal cycle is sensitive to the characteristic differences of the sensor suites used, even
367 if the differences are smaller in the daily mean. This disparity potentially leads to
368 fundamentally different interpretations of the role of clouds in the radiative budget and,
369 in particular, surface melt, which often coincides with the time of the day when the
370 differences are most significant.

371 Despite these discrepancies, both the ICECAPS platform and the DY2 AWS report
372 a positive $E_{net}^{cloud-clear}$. This means that they both describe, on average, higher radiative
373 energy uptake by the surface on cloudy days than on clear-sky days, due to the
374 combination of daytime net shortwave energy absorption, and the hindering of surface
375 longwave radiative losses in cloudy conditions. Our ICECAPS measurements add nuance
376 to this well-known dynamic, the first evidence of higher peak net radiative flux in cloudy
377 conditions than in clear sky conditions. In other words, we show that clouds are not only
378 limiting longwave radiative losses, but can create the conditions for a net radiative flux
379 higher under optically thin clouds than during all the clear sky days of that summer.

380 While these results bring new clarity to the diurnal variability in radiation, the
381 wider Greenland climate science community typically relies on daily albedo to assess and
382 model solar absorption, a practical requirement for both satellite retrievals and modeling.
383 However, results in Fig. 4 show that solely relying on daily mean albedo can mask key
384 physical processes that occur during the diurnal cycle. Despite the demonstrated
385 differences between AWS and ICECAPS radiative fluxes, total time-averaged albedo
386 values agree closely, with mean summer 2024 values of 0.85 (AWS) and 0.86 (ICECAPS).
387 This agreement in daily-mean albedo masks significant differences in the measured total

radiative energy absorbed at the surface at peak solar input in the clear sky state, with important implications for melt. These differences map to a range of complexities, from spectral modification and diffusion of light by clouds or moisture, scattering properties of changing ice sheet surface characteristics across the day, and a strong interdependence on SZA, all of which evolve on sub-daily timescales. For further discussion of this comparison, including assessment of other locations, see Methods: AWS comparison.

Generalizing beyond the diurnal cycle, Figs. 5a and 5b show the two-dimensional distributions of observed longwave and shortwave radiation for the cloudy and clear-sky states. Fig. 5c partitions the contributions of those states relative to the energy accumulated in the near-surface firn, which is measured independently with a subsurface temperature string. The spread of each distribution reflects the variety of atmospheric conditions sampled in each state. For cloudy conditions, cloud LWP is a primary driver of radiative variability[41]. Summer 2024 cloud LWP (Extended Data: Fig. 1) was in the radiatively sensitive regime (LWP<30 $g \cdot m^{-2}$) 55% of the time, with a mean of 26 $g \cdot m^{-2}$.



406

407 **Fig. 5 | Charting the relationships between cloud properties and energy transfer for**
408 **cloudy and clear conditions** with probabilistic distributions of longwave and shortwave
409 states separated by cloudy **(a)** and clear **(b)** conditions. In **(c)**, the cumulative energy
410 accumulation in the upper (20 cm) firn is partitioned by state over time to quantify how
411 these conditions relate to subsurface energy storage.

412

413

414

For clear sky occurrences (Fig. 5b), the distribution of radiative states follows a nearly-linear path. In these cases, increasing net shortwave flux corresponds with decreases in net longwave. This is because shortwave absorption in daytime occurs as warmer air temperatures and solar gain increase surface temperature and thus longwave emission. In this way, without clouds, the radiative budget in clear skies represents the diurnal oscillation from lower nighttime longwave losses to large longwave losses and solar gain in daytime.

Overall, the cloudy state is associated predominantly with near-zero to positive total radiative flux whereas the clear-sky state occurrences primarily relate to negative total radiative flux (Fig. 5). The exceptions for the clear-sky state are the most extreme net shortwave absorption values where the shortwave absorption overcomes the radiative loss at the peak of the solar cycle. As our observations are at a single site, for other locations the character of this relationship will vary with surface temperature, cloud characteristics, snow properties, and sun angle. Realistic representation of the surface radiative budget relationships shown in Fig. 5, and their drivers, is essential for models to simulate the observed radiative conditions and thus project future Greenland melt[45].

Radiation dominates the surface energy budget over the Greenland ice sheet, with turbulent sensible heat flux only overwhelming radiation in rare cases of extreme synoptic heat transport[46,47]. Because radiation is the first order energetic input, the radiative signature of our cloudy and clear-sky states should be apparent in the subsurface energy content. To assess this, Fig. 5c shows cumulative energy content

(Methods: Firn energy calculation) in the upper 20 cm of firn derived from subsurface temperature profiles, partitioned by cloudy and clear-sky states using the same methodology presented above. This approach foregoes the methodological complexity of eddy covariance measurements, bulk flux estimates, and the uncertainties in full energy budget closure[48] in favor of an independent validation of the radiative results. It also demonstrates that the radiative balance observed by ICECAPS, in contrast with the AWS measurement differences, is consistent with energy propagation into the ice sheet.

Over summer 2024, the partitioned energy accumulation in the upper 20 cm of firn (Fig. 5c) was a net gain of 3.4 $MJ \cdot m^{-2}$ during cloudy conditions and a net loss of -2.3 $MJ \cdot m^{-2}$ during clear-sky, with a total energetic gain during the observed period of 1.1 $MJ \cdot m^{-2}$. In addition to these net fluxes, much of the surface energy flux over the summer propagates deeper into the firn via conduction and meltwater percolation. The partitioning of these values is quite similar to the partitioning of mean radiative energy uptake in cloudy (16.6 $W \cdot m^{-2}$) and clear-sky (-9.9 $W \cdot m^{-2}$) conditions, showing that the cloudy-clear partitioned radiative budget maps coherently onto independent subsurface energy measurements. Comparing these subsurface fluxes to the AWS measurements, the average AWS net clear sky radiative flux was reported to be positive, which contradicts the energetic losses observed in the subsurface. While there are other processes at play, the large AWS shortwave fluxes near solar noon should imprint an energetic signature in the subsurface. Notably, the relative magnitude of cloudy-to-clear energy is consistent across these independent measurements: partitioned firn energy (3.4 / -2.3 = -1.48) and mean surface radiative flux (16.6 / -9.9 = -1.68) both yield similar

ratios. This agreement confirms that the observed radiative state differences propagate coherently into the firn.

Together, these observations demonstrate that cloudy conditions drive large positive radiative fluxes at the surface that correspond with firn energy gains. Conversely, clear-sky radiative losses correspond with firn energy loss. While these summer 2024 measurements provide constraints on these key processes, the disparities with AWS radiation measurements and the uncertain role of clouds documented in the literature highlight an urgent need for sustained, long-term observations spanning seasons and years to further constrain cloud properties, ice sheet surface characteristics, and the processes that drive surface melt. Such information would be of immense value to modeling groups who rely on a wide range of data, from AWS measurements to satellite retrievals to targeted in situ studies, to improve their physical schemes and thus their predictive capability for both short-term forecasts and climate projections.

Understanding Greenland's future

The measurements presented here detail how clouds modify Greenland's energy balance in a region vital to understanding surface melt. Yet no field campaign, however comprehensive, can observe the ice sheet's future. That requires models that faithfully represent these processes, informed by the observations necessary to constrain them. This synergy will determine our ability to constrain Greenland's melt pathways and thus its future. Here are the most urgent findings from these summer 2024 observations on the lower southwestern ice sheet:

Despite being one of the snowiest and cloudiest summers on record across Greenland, 55% of observed clouds had LWP <30 $g \cdot m^{-2}$, transmitting substantial solar radiation while also efficiently trapping longwave radiation [34]. On average, cloudy skies produced a total surface radiation of 16.6 $W \cdot m^{-2}$ versus -9.9 $W \cdot m^{-2}$ of radiative loss under clear skies, producing a mean cloudy state radiative effect of 26.5 $W \cdot m^{-2}$. The peak in net surface radiation, near solar noon when melt is most likely, was 80% larger for cloudy (63 $W \cdot m^{-2}$) than clear-sky conditions (35 $W \cdot m^{-2}$). Independent firn energy measurements confirm that this radiation propagates into the upper firn (20 cm), with 3.4 $MJ \cdot m^{-2}$ of energy retained under cloudy conditions versus -2.3 $MJ \cdot m^{-2}$ lost under clear skies. Together, these observations independently verify that energy transmission into the firn occurred predominantly in cloudy conditions during summer 2024 across the diurnal cycle.

Comparison with nearby AWS measurements revealed differences in clear-sky radiative fluxes, indicating that the current monitoring infrastructure may overestimate the importance of clear-sky solar transmission. Crucially, the AWS-measured total radiative flux was twice that of ICECAPS at solar noon (39 $W \cdot m^{-2}$ higher) in clear skies. Current solar measurement strategies for remote Greenland deployment are optimized for daily mean accuracy rather than diurnal fidelity, a fact that influences interpretation of critical energetic processes. However, these results demonstrate that because melt preferentially occurs near the daily peak in solar irradiance, better constraints are needed on measurement uncertainty throughout the daily cycle. Prior AWS studies report near-zero or marginally negative cloud radiative effects at low albedo coastal sites [49,50], but the differences demonstrated here indicate that clouds likely play a larger role in the

ice sheet energy budget than previously realized. As melt moves up the ice sheet, the interior will eventually resemble the observations presented here, and so the physics of melt here today is critical to forecasting the fate of the Greenland interior tomorrow.

Surface albedo, cloud properties, and elevation all change considerably across the ice sheet, and with them the radiative balance between cloudy and clear-sky states. Over bare ice at lower elevations, reduced albedo broadens the range of shortwave absorption while different cloud regimes alter the longwave balance. Understanding how these relationships vary across elevations, surface types, and seasons with different snowfall and synoptic forcing demands further synergistic observations in key locations sampling a wide range of conditions.

For models, as melt and runoff zones continue to ascend the ice sheet, these measurements can serve as a benchmark for reproducing the observed cloudy and clear-sky radiative states and their subsurface impacts. But more broadly, this analysis raises questions for the wider Greenland research community: What future observations are needed to address gaps in our understanding of atmosphere-surface interactions and improve predictive skill? How can in situ automated monitoring networks and more sophisticated installations leverage their distinct capabilities to provide the best possible measurements of ice sheet processes spatially?

These questions point to outstanding research needs. Foundational Arctic climate system processes are difficult to measure, model, and project, while large observational uncertainties remain. The upcoming fifth International Polar Year (2032-33) offers a

critical opportunity to make the drivers of Greenland surface melt a core focus and to examine them from a diverse range of perspectives.

Bibliography

1. Trusel, L. D. et al. Nonlinear rise in Greenland runoff in response to post-industrial Arctic warming. *Nature* **564**, 104-108 (2018).
2. Rahlves, C., Goelzer, H., Born, A. & Langebroek, P. M. Historically consistent mass loss projections of the Greenland ice sheet. *Cryosphere* **19**, 1205-1220 (2025).
3. Aschwanden, A. et al. Contribution of the Greenland Ice Sheet to sea level over the next millennium. *Sci. Adv.* **5**, eaav9396 (2019).
4. AMAP. *Arctic Climate Change Update 2021: Key Trends and Impacts. Summary for Policy-makers* (Arctic Monitoring and Assessment Programme, Tromsø, Norway, 2021).
5. Fox-Kemper, B. et al. Ocean, cryosphere and sea level change. In *Climate Change 2021: The Physical Science Basis. Contribution of Working Group I to the Sixth Assessment Report of the Intergovernmental Panel on Climate Change* (eds Masson-Delmotte, V. et al.) Ch. 9 (Cambridge Univ. Press, 2021).
6. Hofer, S., Tedstone, A. J., Fettweis, X. & Bamber, J. L. Cloud microphysics and circulation anomalies control differences in future Greenland melt. *Nat. Clim. Change* **9**, 523-528 (2019).

7. IMBIE Team. Mass balance of the Greenland Ice Sheet from 1992 to 2018. *Nature* **579**, 233-239 (2020).
8. Zeitz, M., Reese, R., Beckmann, J., Krebs-Kanzow, U. & Winkelmann, R. Impact of the melt-albedo feedback on the future evolution of the Greenland Ice Sheet with PISM-dEBM-simple. *Cryosphere* **15**, 5739-5764 (2021).
9. Bonsoms, J., Oliva, M., Alonso-González, E., Revuelto, J. & López-Moreno, J. I. Impact of climate change on snowpack dynamics in coastal Central-Western Greenland. *Sci. Total Environ.* **913**, 169616 (2024).
10. Mostue, I. A., Hofer, S., Storelvmo, T. & Fettweis, X. Cloud- and ice-albedo feedbacks drive greater Greenland Ice Sheet sensitivity to warming in CMIP6 than in CMIP5. *Cryosphere* **18**, 475-488 (2024).
11. Bevis, M. et al. Accelerating changes in ice mass within Greenland, and the ice sheet's sensitivity to atmospheric forcing. *Proc. Natl Acad. Sci. USA* **116**, 1934-1939 (2019).
12. Pinault, J.-L. Weakening of the geostrophic component of the Gulf Stream: a positive feedback loop on the melting of the Arctic ice sheet. *J. Mar. Sci. Eng.* **11**, 1689 (2023).
13. Böning, C. W., Behrens, E., Biastoch, A., Getzlaff, K. & Bamber, J. L. Emerging impact of Greenland meltwater on deepwater formation in the North Atlantic Ocean. *Nat. Geosci.* **9**, 523-527 (2016).
14. Slater, T. et al. Increased variability in Greenland Ice Sheet runoff from satellite observations. *Nat. Commun.* **12**, 6069 (2021).

15. Slater, D. A. & Straneo, F. Submarine melting of glaciers in Greenland amplified by atmospheric warming. *Nat. Geosci.* **15**, 794-799 (2022).
16. Ryan, J. C. et al. Greenland Ice Sheet surface melt amplified by snowline migration and bare ice exposure. *Sci. Adv.* **5**, eaav3738 (2019).
17. Gallagher, M. R., Shupe, M. D., Chepfer, H. & L'Ecuyer, T. Relating snowfall observations to Greenland ice sheet mass changes: an atmospheric circulation perspective. *Cryosphere* **16**, 435-450 (2022).
18. Ryan, J. C. et al. Decreasing surface albedo signifies a growing importance of clouds for Greenland Ice Sheet meltwater production. *Nat. Commun.* **13**, 4205 (2022).
19. Tedstone, A. J. & Machguth, H. Increasing surface runoff from Greenland's firn areas. *Nat. Clim. Change* **12**, 672-676 (2022).
20. Boers, N. & Rypdal, M. Critical slowing down suggests that the western Greenland Ice Sheet is close to a tipping point. *Proc. Natl Acad. Sci. USA* **118**, e2024192118 (2021).
21. Beckmann, J. & Winkelmann, R. Effects of extreme melt events on ice flow and sea level rise of the Greenland Ice Sheet. *Cryosphere* **17**, 3083-3099 (2023).
22. Shupe, M. D. et al. High and Dry: new observations of tropospheric and cloud properties above the Greenland Ice Sheet. *Bull. Am. Meteorol. Soc.* **94**, 169-186 (2013).
23. Mote, T. L. & Mattingly, K. S. *MEaSUREs Greenland surface melt daily 25km EASE-Grid 2.0, Version 1 (JJA 1980-2020)* [Data set]. Zenodo https://doi.org/10.5281/zenodo.7591560 (2023).

24. Mattingly, K. S. et al. Strong summer atmospheric rivers trigger Greenland Ice Sheet melt through spatially varying surface energy balance and cloud regimes. *J. Clim.* **33**, 6809-6832 (2020).
25. Van Tricht, K. et al. Clouds enhance Greenland ice sheet meltwater runoff. *Nat. Commun.* **7**, 10266 (2016).
26. Ryan, J. C., Medley, B., Stevens, C. M., Sutterley, T. C. & Siegfried, M. R. Role of snowfall versus air temperatures for Greenland ice sheet melt-albedo feedbacks. *Earth Space Sci.* **10**, e2023EA003158 (2023).
27. Hofer, S., Tedstone, A. J., Fettweis, X. & Bamber, J. L. Decreasing cloud cover drives the recent mass loss on the Greenland Ice Sheet. *Sci. Adv.* **3**, e1700584 (2017).
28. Bennartz, R. et al. July 2012 Greenland melt extent enhanced by low-level liquid clouds. *Nature* **496**, 83-86 (2013).
29. Glaude, Q. et al. A factor two difference in 21st-century Greenland Ice Sheet surface mass balance projections from three regional climate models under a strong warming scenario (SSP5-8.5). *Geophys. Res. Lett.* **51**, e2024GL111902 (2024).
30. Gallagher, M. R., Chepfer, H., Shupe, M. D. & Guzman, R. Warm temperature extremes across Greenland connected to clouds. *Geophys. Res. Lett.* **47**, e2019GL086059 (2020).
31. Cox, C. J. et al. The De-Icing Comparison Experiment (D-ICE): a study of broadband radiometric measurements under icing conditions in the Arctic. *Atmos. Meas. Tech.* **14**, 1205-1224 (2021).

32. Fair, Z., Flanner, M., Schneider, A. & Skiles, S. M. Sensitivity of modeled snow grain size retrievals to solar geometry, snow particle asphericity, and snowpack impurities. *Cryosphere* **16**, 3801-3814 (2022).
33. Qu, X. & Hall, A. What controls the strength of snow-albedo feedback? *J. Clim.* **20**, 3971-3981 (2007).
34. Shupe, M. D. & Intrieri, J. M. Cloud radiative forcing of the Arctic surface: the influence of cloud properties, surface albedo, and solar zenith angle. *J. Clim.* **17**, 616-628 (2004).
35. Miller, N. B. et al. Surface energy budget responses to radiative forcing at Summit, Greenland. *Cryosphere* **11**, 497-516 (2017).
36. McIlhattan, E. A., L'Ecuyer, T. S. & Miller, N. B. Observational evidence linking Arctic supercooled liquid cloud biases in CESM to snowfall processes. *J. Clim.* **30**, 4477-4495 (2017).
37. Shupe, M. D. et al. The two radiative states of the Arctic atmosphere and their impacts on the surface energy budget of sea ice. *Elementa Sci. Anthr.* **13**, 00100 (2025).
38. Conway, J. P. et al. Cloud forcing of surface energy balance from in situ measurements in diverse mountain glacier environments. *Cryosphere* **16**, 3331-3356 (2022).
39. Stapf, J., Ehrlich, A. & Wendisch, M. Influence of thermodynamic state changes on surface cloud radiative forcing in the Arctic: a comparison of two approaches

using data from AFLUX and SHEBA. *J. Geophys. Res. Atmos.* **126**, e2020JD033589 (2021).

40. Ramanathan, V. et al. Cloud-radiative forcing and climate: results from the Earth Radiation Budget Experiment. *Science* **243**, 57-63 (1989).

41. Intrieri, J. M. et al. An annual cycle of Arctic surface cloud forcing at SHEBA. *J. Geophys. Res.* **107**, 8039 (2002).

42. Wang, W., Zender, C. S. & van As, D. Temporal characteristics of cloud radiative effects on the Greenland Ice Sheet: discoveries from multiyear automatic weather station measurements. *J. Geophys. Res. Atmos.* **123**, 11,348-11,361 (2018).

43. Fausto, R. S. et al. PROMICE | GC-NET automatic weather station data. *Earth Syst. Sci. Data* **18**, 2829-2873 (2026).

44. Blonquist, J. M. & Bugbee, B. Solar, net, and photosynthetic radiation. In *Agroclimatology* (Agronomy Monograph 60) (eds Hatfield, J. L., Sivakumar, M. V. K. & Prueger, J. H.) (American Society of Agronomy, 2018).

45. Lenaerts, J. T. M., Gettelman, A., Van Tricht, K., van Kampenhout, L. & Miller, N. B. Impact of cloud physics on the Greenland Ice Sheet near-surface climate: a study with the Community Atmosphere Model. *J. Geophys. Res. Atmos.* **125**, e2019JD031470 (2020).

46. Fausto, R. S., van As, D., Box, J. E., Colgan, W. & Langen, P. L. Quantifying the surface energy fluxes in south Greenland during the 2012 high melt episodes using in-situ observations. *Front. Earth Sci.* **4**, 82 (2016).

47. Lund, M. et al. Spatiotemporal variability in surface energy balance across tundra, snow and ice in Greenland. *Ambio* **46** (Suppl. 1), 81-93 (2017).
48. van Tiggelen, M. et al. Surface energy balance closure over melting snow and ice from in situ measurements on the Greenland ice sheet. *J. Glaciol.* **70**, e68 (2024).
49. Wang, W., Zender, C. S., van As, D. & Miller, N. B. Spatial distribution of melt season cloud radiative effects over Greenland: evaluating satellite observations, reanalyses, and model simulations against in situ measurements. *J. Geophys. Res. Atmos.* **124**, 57-71 (2019).
50. Hall, D. K. et al. Comparison of satellite-derived and in-situ observations of ice and snow surface temperatures over Greenland. *Remote Sens. Environ.* **112**, 3739-3749 (2008).

Acknowledgements

This research was supported by the National Science Foundation (grants 2137091, 2137083, 2137152, 2137098), the Natural Environment Research Council, National Centre for Earth Observation (grant NE/X002403/1), and NOAA's Physical Sciences Laboratory via NOAA cooperative agreement NA22OAR4320151. Support also came from the Natural Environment Research Council (NERC) Centre for Satellite Data in Environmental Science (SENSE) Centre for Doctoral Training (grant NE/T00939X/1), the Advanced Research and Invention Agency (ARIA) through the Greenland Automated Mass Balance and Boundary Layer Experiment (GAMB2LE; grant SCOP-PR01-P002), and the NERC-funded ICECAPS-MELT project under the NSF GEO-NERC Collaborative

Research programme (grant NE/X002403/1). This work used JASMIN, the UK's collaborative data analysis environment (https://www.jasmin.ac.uk; last accessed 5 June 2026; Lawrence et al., 2013). We acknowledge important field support provided by Ian Geraghty, Polarfield Services, and the New York Air National Guard. This work would not be possible without remarkable teachers. The scientific results and conclusions, as well as any views or opinions expressed herein, are those of the author(s) and do not necessarily reflect the views of NOAA or the Department of Commerce.

Author contributions

M.R.G. led the field project, engineered the autonomous platform and power system, and designed the analysis. M.D.S. and V.P.W. led the ICECAPS program, project conception and interpretation, and field deployment. A.S. developed the analysis methods and contributed to the field campaign. C.J.C. led the conception and engineering of the core instrumentation and data processing and contributed to the analysis. H.G., A.S.M., and R.R.N. made large contributions to the platform design, scientific analysis, field campaign, and general morale. C.P. contributed to data processing, scientific analysis, and writing. E.O. contributed key engineering expertise and led aspects of the field deployment. R.L.H. and D.P. developed the GNSS-IR snow accumulation method and processed those data. M.S.T. contributed to the analysis and led snow pit sampling and firn characterization. L.D.R. contributed key expertise on the radiation measurements and science analysis. R.L.H., L.W. and H.-P.M. designed and built the ground-penetrating radar system and developed the melt-index algorithm. B.V. contributed to the scientific

analysis, PROMICE/GC-Net data analysis, and writing. R.M. contributed to the scientific analysis, as well as regional modeling context and interpretation. K.S.M. contributed to the scientific analysis and field deployment. D.C.-S. contributed to the scientific analysis and firn discussion. C.H. provided lifeline engineering expertise, field health and safety, and led aspects of the deployment. All authors discussed these results and approved the manuscript.

Competing interests

The authors declare no competing interests.

Data availability

The ICECAPS observational data presented in this study are archived at the Arctic Data Center (https://doi.org/10.18739/A2FT8DM7X) and CEDA (https://catalogue.ceda.ac.uk/uuid/70c96882916149658752b2b123931a5d/). PROMICE/GC-Net automatic weather station data are publicly available from the Geological Survey of Denmark and Greenland via the PROMICE Data Portal (https://promice.org/download-data/) and are described in Fausto et al.[43]. MEaSUREs Greenland surface melt data used for Fig. 1 are available at Zenodo (https://doi.org/10.5281/zenodo.7591560).

Code availability

Custom codes used in this study, including the basic data processing pipeline, ground-penetrating radar melt-index algorithm, microwave radiometer processing (MWRRET implementation per Turner et al.[55]), and firn energy calculation, are available from the corresponding author on request. GNSS interferometric reflectometry processing was performed using the open-source gnssrefl toolbox following Pickell et al.[54]. Surface flux processing followed the methodology of Cox et al.[51].

Methods

Autonomous research platform

The platform deployed in summer 2024 was designed to make coupled atmosphere-surface-subsurface observations where surface melt regularly occurs and percolates into the firn. Five team members installed the platform over four weeks in early May 2024, after which the system operated autonomously until August 2024. Select realtime-processed scientific data and system diagnostic information were transmitted via satellite link in hourly intervals for monitoring, diagnostics, and operation.

The platform was powered exclusively by a renewable energy power system, consisting of 16 solar panels providing 8 kW of peak generation and four wind microturbines rated at 1.6 kW combined. The generated energy was stored in a modular lithium battery bank totaling 30 kWh. Individual battery modules were housed in insulated enclosures with heating and managed feedback with the power generation

system. The wind turbines provided supplemental power for approximately one month before mechanical failure, but the solar array alone proved sufficient for sustained operation. Post-campaign analysis indicated the platform could have operated on roughly half the installed storage and generation capacity, informing future deployments.

The instrument suite comprised more than 20 distinct instruments with approximately 100 sensors spanning the subsurface, surface, and atmospheric column. The suite can be broken down into three packages: the surface flux suite targeting surface properties and energy fluxes, expanding on the “Atmospheric Surface Flux Station” (ASFS) from the year-long “MOSAiC” sea ice campaign [51] ; the profiling suite including vertically pointing high atmospheric remote sensing cloud, and precipitation instruments; and the sub-surface suite including measurements of firn characteristics both from sensors in real time as well as strategic sampling at platform install and demobilization. The processes driving surface melt span the atmospheric column to the upper firn, crossing traditional disciplinary boundaries. The methods below document each component to make explicit the holistic observations that went into this snapshot of the coupled melt processes presented here, although not all feature prominently in the descriptive conclusions of the paper.

Instrument / Model	Variable(s) Measured	Uncertainty
Atmospheric measurements		
METEK MRR-Pro	Precipitation radar reflectivity profiles and retrieved precipitation fall rates	varr.[59]
Vaisala CL61	Cloud base height, depolarization lidar backscatter profiles	varr.[58]
Radiometer Physics HATPRO	Integrated atmospheric brightness temperatures; retrieved cloud liquid water path (LWP) and precipitable water vapor (PWV)	LWP: 15 $g \cdot m^{-2}$
Handix Scientific Portable Optical Spectrometer	Aerosol size distribution and concentration	0.83 cm
Surface Radiation Fluxes		
Hukseflux SR30 pyranometers (↑↓), heated/ventilated	Broadband shortwave radiation (up/downwelling)	3.1 $W \cdot m^{-2}$
Hukseflux IR20 pyrgeometers (↑↓), heated/ventilated	Broadband longwave radiation (up/downwelling) and derived surface skin temperature (T_skin[52])	LW↑: ±1 $W \cdot m^{-2}$; LW↓: ±2.6 $W \cdot m^{-2}$
Delta-T SPN1 pyranometer (shaded/unshaded)	Direct and diffuse shortwave partitioning	5% or 10 $W \cdot m^{-2}$
Meteorology and Turbulent Fluxes		
Metek u-sonic 3D sonic anemometer (3.8 m)	Rapid 3D winds and turbulent fluxes (eddy covariance and bulk derived)	0.3 m s^{-1}
Licor LI-7500ds laser gas analyzer	Rapid water vapor measurements for turbulent latent heat fluxes	2 $W \cdot m^{-2}$ in LHF
Vaisala PTU307 T/RH/P meteorology sensor (2 m)	Air temperature, relative humidity, pressure	T: 0.3-0.4°C RH: 1.6-1.8%; P: 0.15 hPa
Apogee S111s infrared thermometer (↓)	Surface brightness temperature, independent measure	0.12-0.14°C
Surface Height and Accumulation		
Campbell SR50 acoustic sounder	Surface height change (point)	1.2 cm
R.M. Young SnoDAR laser distance sensor	Surface height change (point)	1 cm
OGRE GNSS receivers	Snow accumulation, surface roughness (GNSS-IR)	0.9 cm

Instrument / Model	Variable(s) Measured	Uncertainty
Firn properties		
SAMS SIMBA DS18B20 digital temperature string	Firn temperature profiles (2 cm vertical, 15 min temporal)	2°C;
Hukseflux HFP01 heat flux plates	Subsurface conductive energy flux (25, 50, 100 cm depths)	3%
Custom ground-penetrating radar (5.4, 7.7 GHz)	Firn structure and retrieved liquid water presence (melt index from signal attenuation)	Melt index threshold: 0.6
Other Auxiliary		
4× visible photo cameras (15 min interval)	Visual instrument state monitoring; sky/surface conditions	N/A
Snow sampling	Snow pits and stratigraphy transects	varr.[52]
Hardware diagnostic information	Misc sensors for compute, power generation, and other onboard platform diagnostics	N/A

Table 1. ICECAPS autonomous instrument suite, summer 2024.

Most variables recorded at 1-minute temporal resolution unless otherwise noted, measurements made on the southwestern Greenland ice sheet (66.48°N, 46.30°W, 2094 m a.s.l.). For a photo of the instrument suite, see Extended Data Fig. 9.

Data processing

Data processing for the surface flux measurements follows the methodology established for the ASFS platforms during MOSAiC[51] with adaptations for the Greenland deployment and additional atmospheric profiling instruments. The majority of parameters are measured as 1-minute averages while eddy covariance sensors operate at 20 Hz. Flux calculations are standardized to 10-minute windows and integrated using eddy covariance methods. To accurately measure radiative fluxes, shortwave sensors are corrected for tilt using inclinometer data and compared to direct and diffuse components from the collocated shaded pyranometer. Longwave radiation is corrected for a solar heating bias of the downward-facing pyrgeometer dome following the regression approach described in Sledd et al. 2026[52]. The bias is related to upwelling shortwave flux

incident on the sensor and is quantified during confirmed melt conditions (GPR melt index ≥ 0.6, air temperature > 0 °C). The corrected upwelling longwave radiative flux is then used to derive surface skin temperature assuming a snow emissivity of 0.985 [60], yielding an uncertainty of ±0.4°C. Albedo is calculated from the ratio of upwelling to downwelling shortwave radiative fluxes, restricted to solar zenith angles < 80° to minimize measurement artifacts at low sun angles.

Meteorological observations include shielded temperature and humidity at 2 m and three-dimensional winds from a sonic anemometer at 3.8 m. Turbulent sensible heat flux is computed from 20 Hz sonic anemometer data using the eddy covariance method, with quality control for flow distortion sectors, stationarity, and integral turbulence characteristics following the procedures in Cox et al. (2023)[51]. Bulk flux estimates of sensible and latent heat are also computed from gradient measurements using Monin-Obukhov similarity theory with the COARE algorithm adapted for stable conditions over ice[61,62]. A comprehensive treatment of the complete energy budget including turbulent flux measurements and closure is deferred to forthcoming work.

Atmospheric profiling instruments undergo instrument-specific processing. Cloud liquid water path (LWP) and precipitable water vapor (PWV) are retrieved from microwave radiometer brightness temperatures at 23.8 and 31.4 GHz following the ARM Microwave Radiometer Retrieval (MWRRET) algorithm[55,56]. The MWRRET approach uses a physical optimal estimation retrieval that applies brightness temperature offsets to reduce spurious LWP bias under clear skies, providing improved retrievals over statistical coefficient methods (see Methods: Measuring Liquid Water Path for more detail). Cloud

base height from the CL61 lidar is used as input to constrain the temperature of liquid water layers in the retrieval. Cloud presence and base height are determined from the Vaisala CL61 ceilometer-lidar using an algorithm that identifies cloud layers by backscatter coefficient thresholds. Depolarization ratio measurements by this system also provide information on cloud phase. Precipitation occurrence and reflectivity profiles are obtained from the METEK MRR-Pro micro rain radar, which operates at 24 GHz (K-band) and profiles from approximately 100 m to several kilometers above the surface.

Surface height and snow accumulation are measured using three independent methods. An acoustic sounder and a laser distance sensor provide point measurements of surface height change at key points on the platform, below downward facing radiation sensors and at the GPR. Additionally, multiple GNSS receivers provide spatially integrated estimates of snow accumulation and surface roughness through GNSS interferometric reflectometry (GNSS-IR), following the methodology developed by Pickell et al.[54]. The three methods differ in spatial footprint and are used together to characterize both the local surface evolution and its spatial variability.

Subsurface firn temperature observations are processed following Sledd et al. (2026)[52]. Temperature profiles from the digital temperature string (2 cm vertical resolution, 15-minute sampling) are corrected for solar heating bias using an empirical relationship between above-zero subsurface temperatures and transmitted shortwave radiation estimated from Beer's law (extinction coefficient κ = 19 m^{-1}, NIR fraction f = 0.5). The surface height within the temperature string is identified from the maximum

variance of the vertical temperature gradient in 24-hour windows. Firn energy content in the upper 20 cm is calculated from temperature profiles using measured density interpolated from snow pits conducted at install and decommissioning of the site (Town et al. 2026a,b,c,d). The ground-penetrating radar provides a melt index derived from 5.4 GHz signal attenuation, where values exceeding 0.6 indicate liquid water presence in the firn and are used to confirm melt timing identified from skin temperature and subsurface temperature convergence at 0 °C.

Data are archived and freely available at the Arctic Data Center.

Measuring Liquid Water Path (LWP)

Cloud liquid water path is a first-order control on the Arctic surface radiative budget, governing the balance of cloud longwave emission and shortwave transmission that makes the surface radiative balance particularly sensitive to thin clouds (Shupe and Intrieri 2004; Miller et al. 2015). Thus, while the measurement is costly in terms of power and footprint, MWR measurements are essential for our understanding of surface energy flux processes. We retrieve LWP and precipitable water vapor (PWV) from zenith brightness temperature measurements at 23.8 and 31.4 GHz using the physical optimal estimation framework of the ARM Microwave Radiometer Retrieval (MWRRET) algorithm. Water vapor emission dominates the 23.8 GHz channel, positioned on the wing of the 22.2 GHz water vapor absorption line, while liquid water emission constitutes the primary signal at 31.4 GHz. The MWRRET retrieval applies brightness temperature offsets to the 23.8 GHz channel to reduce systematic biases in clear-sky

LWP that arise from uncertainties in the microwave absorption model, and uses cloud base height from the collocated CL61 lidar to constrain the temperature of liquid water layers in the retrieval.

The fundamental challenge for this measurement is that standard 2-channel MWR LWP uncertainty[55] is approximately 25 g m^{-2} which is roughly equal to the LWP values of greatest radiative importance in this study. LWP sensitivity to clouds with low liquid water content is limited by the roughly linear relationship between 31.4 GHz brightness temperature and LWP, which yields a noise floor of approximately 12 gm $^{-2}$ from instrument radiometric uncertainty alone[56]. But while LWP at a given moment in time is relatively uncertain, the sampling of these measurements as distributions provides a consistent understanding of cloud liquid characteristics. In comparison, the ICECAPS observatory at Summit Station achieved significantly lower LWP uncertainty (~3 g·m^{-2}) by combining the standard HATPRO channels with high-frequency measurements at 90 and 150 GHz, which increase sensitivity to baseline LWP[34]. These additional channels were not available on the ICECAPS-MELT platform due to power constraints of the autonomous deployment. Consequently, the LWP values reported here carry larger uncertainties than those from Summit. Despite these limitations, the MWRRET retrieval provides the only continuous, ground-based measure of cloud liquid water on the Greenland ice sheet outside of Summit Station. The distributions and relationships presented in this study (Figs. 4, 5) should be interpreted with these uncertainties in mind, noting that individual LWP values below ~25 g·m^{-2} are within the retrieval uncertainty while the statistical distributions from the full summer record remain robust.

Firn energy calculation

The energy content of the upper firn provides an independent measure of how clouds' radiative impacts influence surface warming and cooling. Because these energetic shifts are rapid at the uppermost layer just beneath the skin, the differences in internal energy were calculated across short timesteps for the upper 20 cm. This parameter is roughly similar to glaciological assessments of "cold content", defined as the energy required to raise the firn temperature to the melting point[57], although cold content is evaluated over the upper 10-20 meters of firn to assess meltwater refreezing potential over seasonal and multi-year timescales. Here we name and discuss this calculation as the energetic changes and accumulation over time partitioned by cloudy and clear conditions.

The energy content in the upper 20 cm of firn is calculated from corrected subsurface temperature profiles (Sledd et al., 2026)[52] following:

$$U = \rho c_i \Delta z (\delta T/\delta t)$$

where ρ is the mean density of the slab, c_i is the heat capacity of ice, Δz is the slab thickness (20 cm), and $\delta T/\delta t$ is the temporal temperature change computed using centered differencing. Density is derived from manual measurements taken during snow pits at installation and decommissioning (Town et al. 2026a,b,c,d), with fresh snow assumed to have a density of 150 $kg \cdot m^{-3}$. The change in energy is then accumulated over time to produce the cumulative energy content shown in Fig. 5c.

To attribute firn energy changes to atmospheric state, the cumulative energy is partitioned by the cloudy and clear sky classification determined from the lidar-based cloud identification (Methods: Cloud identification). The resulting partitioned time series (Fig. 5c) show how much energy was gained or lost by the upper 20 cm during each state over the course of the summer.

There are several important caveats. The 20 cm depth is chosen to capture the layer most responsive to atmospheric forcing on diurnal timescales while limiting sensitivity to spatial variability in ice lens distribution between the temperature string location and snow pit site. Deeper energy fluxes from conduction and meltwater percolation are not captured in this shallow integral. Density uncertainty is the dominant source of error; even modest errors in density propagate through the thermal conductivity parameterization and accumulate over the season (Sledd et al., 2026 [52], their Fig. 11). Nevertheless, the coherence between the partitioned firn energy and the independently measured surface radiative fluxes provides confidence that in bulk, the radiative state differences observed at the surface propagate into the subsurface in a physically consistent manner.

Identifying melt with 5Ghz GPR

The continuously operating Ground Penetrating Radar (GPR) was designed around the Novelda X4 chip, and included some additional analog filters and amplifiers. We used ultrawideband QPar horn antennas with waveguides, and an embedded BeagleBone Black CPU. This system was modified from the tower mounted system used previously

over seasonal snow (e.g., Brangers et al., 2024 [63]), and was operated at center frequencies of 5.4 GHz and 7.7 GHz, with a bandwidth of approximately 1.5 GHz. This GPR is an ultrawideband impulse radar that uses a delta-sigma Analog-to-Digital Converter (ADC), using many repeated measurements with small time shifts that are less than the sample interval, to build a full waveform. These full waveforms are then averaged to improve the Signal-to-Noise Ratio (SNR) over a period of approximately 2 minutes, and this averaged waveform is stored every 15 minutes. The radar was mounted with the antennas oriented perpendicular to the snow surface, to observe stratigraphy, snow accumulation and snow melt.

At these relatively short wavelengths (3-5 cm), when there is surface melt, the majority of the radar signal is reflected from and absorbed within the surface wet layer, and stratigraphy is no longer visible. When the surface snow refreezes, the deeper stratigraphy is once again visible. We use this effect to detect periods of surface melt. We first preprocess the raw radar waveforms with a sky calibration to remove transmitter artifacts, a bandpass filter to remove noise, and a linear range gain to offset the effect of signal spreading on return power. The resulting radargram clearly shows the subsurface stratigraphy, and in particular a strong reflector at 1.5-2 m depth, which we interpret as the last summer surface (LSS), a strong dielectric contrast created by the refrozen previous summer melt overlain by winter snowfall.

To construct our Melt Probability Index, we integrate the returned radar power across the LSS for each waveform. During periods of melt, where the melt obscures the LSS, the return power is low, and during dry periods the return power is high. We then invert and scale the integrated power to a range [0 1] in which 0 indicates the lowest

probability of melt and 1 indicates the highest probability of melt. For the purposes of analysis, values larger than 0.8 were empirically determined (using contemporaneous data from other sensors: firn temperature, subsurface flux plates, and cameras) to be attenuation caused by the presence of liquid water.

Cloud identification

This analysis partitions observations into cloudy and clear sky (cloud-free) atmospheric states to quantify the atmospheric state effect of clouds on surface radiation ($E^{clouds}(Q_{net})$ in this analysis) and firn energy. This classification uses vertically integrated attenuated backscatter from the Vaisala CL61 ceilometer-lidar as the primary discriminator. The integrated backscatter exhibits a stark bimodal distribution with a division at approximately 10^{-4} m^{-1} sr^{-1}, corresponding to the separation between cloud-free atmospheric scattering and scattering from overhead cloud layers.

The resulting classification was validated against auxiliary observations including microwave radiometer LWP retrievals (where LWP > 5 $g \cdot m^{-2}$ indicates liquid-bearing cloud), camera imagery, and direct versus diffuse incoming solar radiation, all of which show strong consistency with the lidar-based partitioning. This binary classification was chosen deliberately for simplicity and ease of interpretation. The stark bimodality in the backscatter distribution and the coherent results across independent measurements (radiation, LWP, firn energy) confirm that this simple partitioning captures the first-order separation between the two observed radiative regimes.

Synoptic context for melt events

The two melt events for this analysis were selected to illustrate distinct mechanisms of cloudy and clear sky melt as observed in summer 2024 and not to represent a canonical example of melt climatology at this site. These cases are presented because they demonstrate contrasting physical pathways of surface energy gain under the two atmospheric states detailed in this study. To connect the observed surface processes to the large-scale circulation that produced them, we briefly describe the synoptic conditions for each event.

The atmospheric dynamics that led to the June 16th clear sky melt event were a combination of near-surface warm air advection and subsidence aloft. Between the 11th and the 13th, a surface low pressure system transited across the southern tip, advecting with it elevated temperatures in the low-to middle atmosphere (850-700 hPa). After its passing, from the 13th through the 16th, there was weak near surface advection combined with a broad stagnant high pressure system aloft above 500 hPa and consistent maximal solar flux. Transitioning into the melt event on the 16th, a strong low pressure system impinged on the western coast of Greenland leading ahead with strong southerly advection of warm air near the surface. Temperatures elevated while clear skies and large solar fluxes remained as water vapor near the core of this low pressure system lagged behind the warm front. Around solar noon the elevated temperatures and clear skies combined to create a roughly 6 hour period of melt until evening. In daytime on the 17th water vapor, clouds, and temperatures around -2 °C reached the measurement site and the melt event concluded.

For the cloudy event on June 28th, the sustained melt was preceded by a vertically connected and stacked (850 hPa through 400 hPa) low pressure system with the core to the west of the central Greenland ice sheet. Water vapor was anomalously elevated broadly in the region ahead of this system with the sustained advection. This low pressure system strengthened from the 24th through the 27th and slowly moved eastward until the core of the system met with the steep topography of the east coast. On the evening of the 27th through the 28th cyclolysis led to the dissolution of this integrated low while the associated warm and moist air blanketed the region. This warm and cloudy air then led to sustained melt from the combined effects of elevated temperature, longwave blanketing, and the muted transmission of solar to the surface through the clouds.

These synoptic conditions are, in broad strokes, consistent with established descriptive patterns of Greenland melt. Clear sky melt events on the interior ice sheet are typically associated with similar persistent high-pressure systems that allow sustained solar heating over multiple days and residual warm temperatures. Cloudy melt events in southwestern Greenland are commonly linked to cyclonic moisture transport from the North Atlantic along pathways documented in the melt climatology literature (Mattingly et al. 2020) where large atmospheric rivers blanket the region in warm wet air masses.

Snow accumulation and surface roughness

Accurate characterization of snow accumulation, ablation, and surface roughness is essential for interpreting the changes in firn across the period of study. Surface height changes modify albedo through fresh snow deposition, alter the thermal structure of the

upper firn, and reflect the integrated effect of precipitation, sublimation, wind redistribution, and melt. Because these processes exhibit spatial variability even over short distances, the platform employed three independent and complementary measurement approaches. Point measurements of surface height change were made by an acoustic sounder and a laser distance sensor mounted on the platform structure. These instruments provide high temporal resolution (1-minute) records of surface height at their respective measurement points but sample only a narrow column beneath the sensor. Accurate surface measurements can differ from one another by tens of centimeters at times due to spatial heterogeneity of snow distribution, particularly following accumulation or wind redistribution events.

To provide spatially integrated context for these point measurements, three OGRE (Open GNSS Receiver Experiment) multi-GNSS receivers[54] were deployed in a triangular configuration away from the platform. Each OGRE collects hundreds of reflected GNSS signal measurements per day across nearly all azimuths, with the reflected signal sampling an annular footprint around the antenna at meter scales. Daily mean surface height is computed by averaging these measurements over each 24-hour period, yielding a spatially representative estimate with a detectable change threshold of approximately 0.7 cm at daily resolution. Sub-daily surface height trends are identified when any station exhibits a statistically significant ($p < 0.01$) change exceeding 2.5 cm within a given day, enabling detection of active accumulation or ablation periods. Reflectometry heights are processed using the open-source gnssrefl toolbox with parameters following Pickell et al. (2025)[54]. Antenna elevations are derived from Natural Resources Canada CSRS precise point positioning, and surface elevation is calculated by subtracting the mean

reflectometry height from the antenna elevation, reported in the ITRF20/GRS80 reference frame.

The GNSS-IR measurements also provide an experimental estimate of meter-scale surface roughness derived from the variance of reflectometry heights within each daily measurement set[54]. These roughness estimates are a novel measure of spatial surface changes and instrument variability (Extended Data: Fig. 8) and offer a first-order indicator of periods with enhanced surface modification from wind erosion, deposition, or melt-refreeze processes. Over summer 2024, the OGRE surface elevation record shows a net increase, indicating that snow accumulation outpaced the combined effects of firn compaction, ice dynamic thinning, and surface lowering from melt. The accumulation record from the OGREs provides critical spatial context for atmospheric process impacting the surface alongside point-based surface height measurements, particularly during the large accumulation events (e.g., 10-15 cm on June 27-29) that modified surface albedo and insulated the upper firn.

AWS comparison

The PROMICE/GC-Net network operated by the Geological Survey of Denmark and Greenland (GEUS) provides the only spatially distributed, year-round surface measurements across the ice sheet. Spatial assessments of cloud radiative effects over Greenland (e.g., Wang et al. 2018; van Tricht et al. 2016; Conway et al. 2022) rely on AWS radiation measurements as their observational foundation.

Because of the scientific importance of these AWS measurements, the summer 2024 measurement site was strategically chosen to be near the GEUS DY2 AWS. This

station is equipped with a class C Kipp and Zonen CNR4 net radiometer that measures the four broadband radiative flux components (shortwave up/down, longwave up/down) in a single integrated unit. Unlike the ICECAPS sensors, the AWS radiometers are not heated or ventilated, and operate on a strict power budget designed for year-round autonomous operation. The AWS data used here are from the new standard PROMICE data product, including tilt correction for the CNR4 sensors[43]. The differences in shortwave radiation measurements between the two systems are within the specification differences of Class A and Class C instruments, particularly related to zero offset and directional response uncertainties with respect to ISO 9060:2018 standards.

The co-located datasets provide a unique opportunity to assess the AWS radiation measurements against the ICECAPS heated and ventilated class A Hukseflux sensors. Both datasets are analyzed on common 10-minute intervals, and the same cloudy/clear sky partitioning derived from the ICECAPS lidar is applied to both. At the <2km separation distance, this cloud partition was tested and is self-consistent with the PROMICE longwave-derived cloud cover metric. Over 10-minute intervals, both systems see the same sky, such that differences in the partitioned radiative fluxes arise from the measurements themselves. The critical differences in the mean net clear sky radiative fluxes shown in the main text can be characterized in further detail by their probability frequency distributions (Extended Data: Fig. 5a and 5b) as well as the character in the scatter plots of components. Extended Data Figs 3, 4, and 6 step through the aspects of these differences in more detail than the main text can allow.

The shortwave flux around solar noon that results in the differences of absorbed solar energy at peak melt is best described as a difference in albedo as a function of

incoming shortwave radiation measured for each radiation sensor suite (Extended Data Fig. 4). At large incoming solar radiation values, these small differences in measured albedo result in large differences in net magnitudes of radiative flux. For the AWS CNR4 sensors, that manifests as an albedo near 0.81 at maximal incoming shortwave flux whereas for the ICECAPS sensors at these values albedo is near 0.84. Extended Data Figs. 3, 4, and 6 then show that these albedo differences relate to a 30% difference in the measured absorbed net shortwave which, when combined with the other radiative components, creates a factor of two difference in the measured net radiative energy near solar noon.

To support this local comparison of sensors and its application to the broader AWS, Extended Data Fig. 7 demonstrates this difference in albedo for clear skies for both platforms. While it's not possible to directly assess other locations across the ice sheet without more measurement campaigns, Extended Data Fig. 7 shows a brief time period of cloudy and clear sky data from the critical k-transect AWS station KAN_M, as in Figs. 4 and 5. In this Figure similar features of decreasing albedo with increasing incoming shortwave can be seen, during a time period with consistent surface characteristics.

Outside these differences, the rough agreement in mean daily albedo values highlights that the common usage of daily mean albedo and daily mean net radiation to understand Greenland's surface energy budget can mask sub-daily features with significant implications for understanding melt processes. For studies that depend on the diurnal cycle of clear sky radiation, or on the magnitude of cloud radiative effects derived from flux differences, the sensor-level discrepancies documented here are large enough to warrant careful consideration.

Methods Bibliography

51. Cox, C. J. et al. Continuous observations of the surface energy budget and meteorology over the Arctic sea ice during MOSAiC. *Sci. Data* **10**, 519 (2023).
52. Sledd, A. et al. Summer subsurface temperature variability in the percolation zone of southwest Greenland: high resolution observations of the top meter of firn. Preprint at https://doi.org/10.5194/egusphere-2026-1842 (2026).
53. Pickell, D. J. & Hawley, R. L. Performance characterization of a new, low-cost multi-GNSS instrument for the cryosphere. *J. Glaciol.* **70**, e41 (2024).
54. Pickell, D. J., Hawley, R. L. & LeWinter, A. Spatiotemporal patterns of accumulation and surface roughness in interior Greenland with a GNSS-IR network. *Cryosphere* **19**, 1013-1029 (2025).
55. Turner, D. D. et al. Retrieving liquid water path and precipitable water vapor from the Atmospheric Radiation Measurement (ARM) microwave radiometers. *IEEE Trans. Geosci. Remote Sens.* **45**, 3680-3690 (2007).
56. Cadeddu, M. P., Liljegren, J. C. & Turner, D. D. The Atmospheric Radiation Measurement (ARM) program network of microwave radiometers: instrumentation, data, and retrievals. *Atmos. Meas. Tech.* **6**, 2359-2372 (2013).
57. Vandecrux, B. et al. Firn cold content evolution at nine sites on the Greenland ice sheet between 1998 and 2017. *J. Glaciol.* **66**, 591-602 (2020).
58. Le, V., O'Connor, E. J., Filioglou, M. & Vakkari, V. Operational performance of the Vaisala CL61 ceilometer for atmospheric profiling. Preprint at https://doi.org/10.5194/egusphere-2025-6331 (2026).

59. Ferrone, A., Billault-Roux, A.-C. & Berne, A. ERUO: a spectral processing routine for the Micro Rain Radar PRO (MRR-PRO). *Atmos. Meas. Tech.* **15**, 3569-3592 (2022).

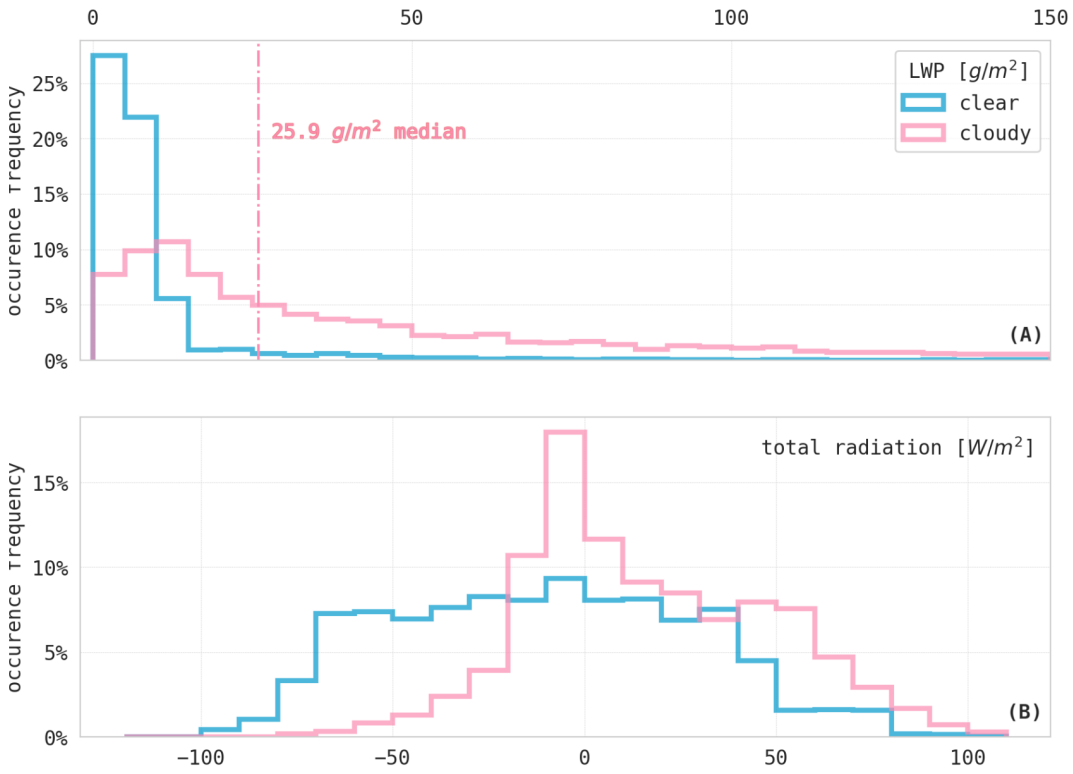
60. Warren, S. G. Optical properties of ice and snow. *Phil. Trans. R. Soc. A* **377**, 20180161 (2019).

61. Fairall, C. W., Bradley, E. F., Hare, J. E., Grachev, A. A. & Edson, J. B. Bulk parameterization of air–sea fluxes: updates and verification for the COARE algorithm. *J. Clim.* **16**, 571–591 (2003).

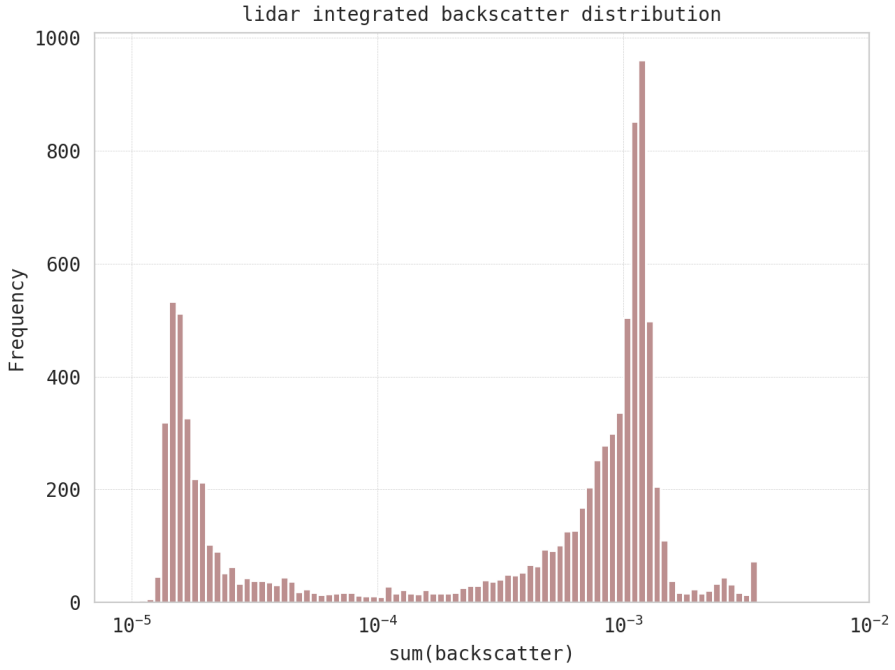
62. Grachev, A. A., Andreas, E. L., Fairall, C. W., Guest, P. S. & Persson, P. O. G. SHEBA flux-profile relationships in the stable atmospheric boundary layer. *Bound.-Layer Meteorol.* **124**, 315–333 (2007).

63. Brangers, I., Marshall, H.-P., De Lannoy, G., Dunmire, D., Mätzler, C. & Lievens, H. Tower-based C-band radar measurements of an alpine snowpack. *Cryosphere* **18**, 3177–3193 (2024).

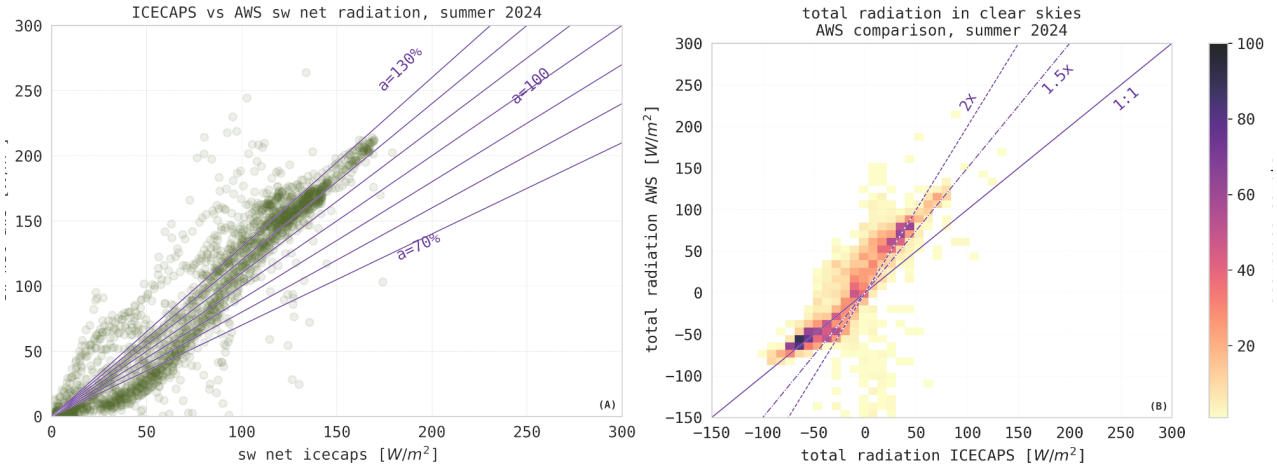
Extended Data



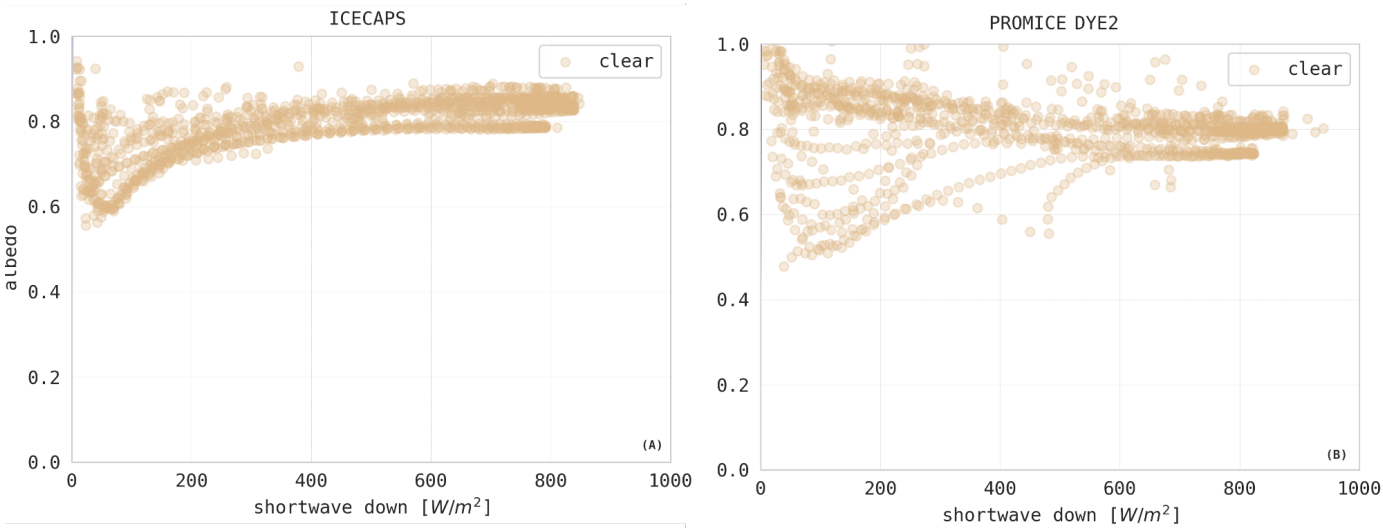
Extended Data Fig. 1 | Observed distributions of liquid water path and net radiation from the summer of 2024 near DYE-2. These distributions show the relative atmospheric liquid water characteristics for the cloudy identified cloudy and clear states and their connection to the net radiation.



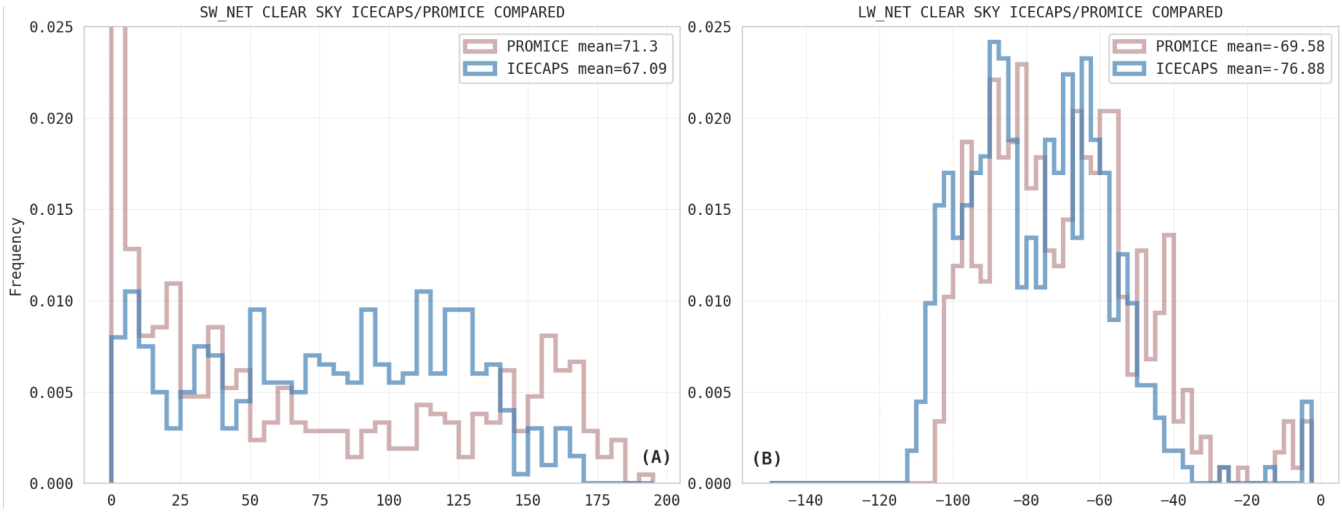
Extended Data Fig. 2 | The log-linear distribution of observed integrated instantaneous lidar backscatter values from the summer of 2024 near DYE-2. The sharp bimodal character was used to separate cloudy and clear conditions for our analysis at a threshold of 10^{-4}.



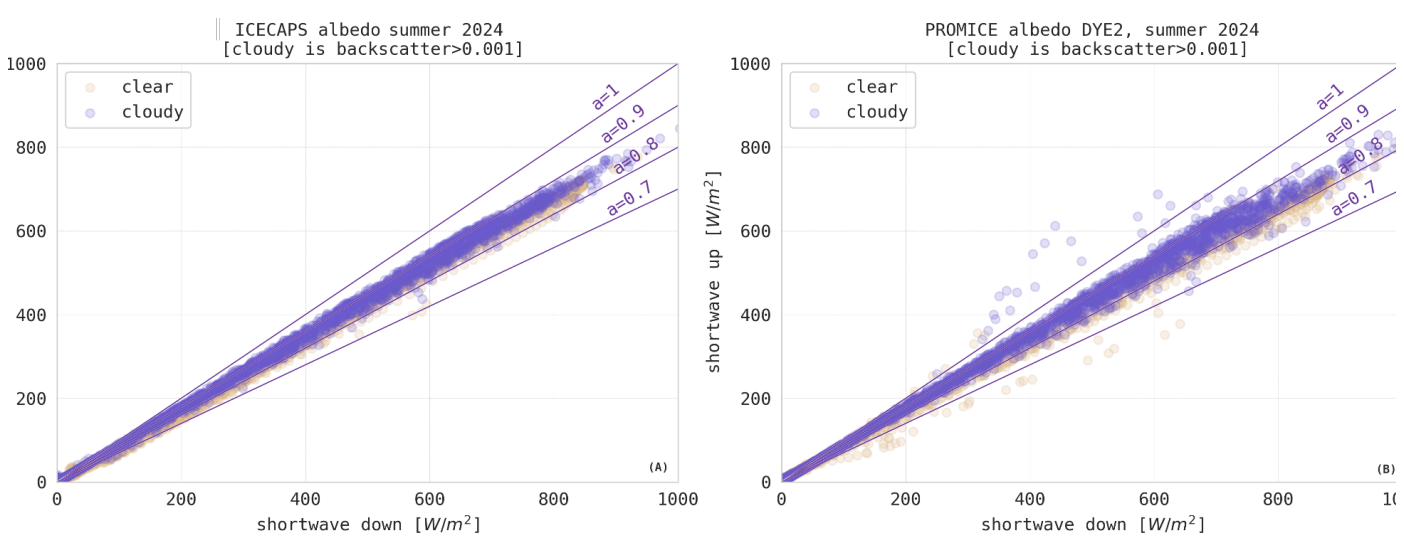
Extended Data Fig. 3 | A comparison of the (a) shortwave for all data and (b) net total radiation for clear skies from the ICECAPS and AWS measurements showing the differing net shortwave at the surface at large values and the corresponding impact on the net total radiation.



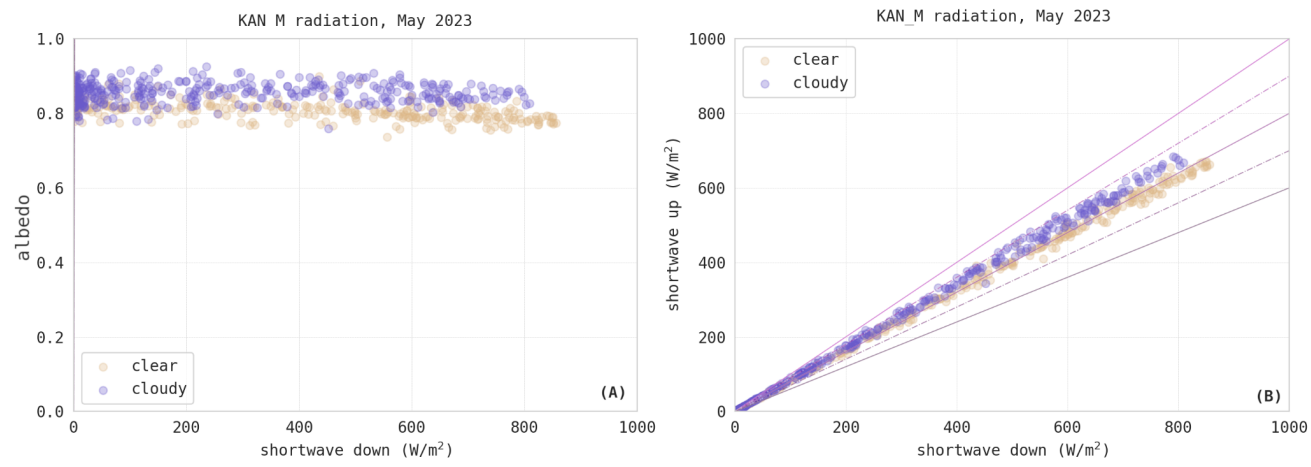
Extended Data Fig. 4 | Albedo plotted against incoming shortwave radiation for clear skies from the **(a)** ICECAPS and **(b)** AWS showing the characteristic signature of decreasing albedo with increasing incoming shortwave for the AWS sensor.



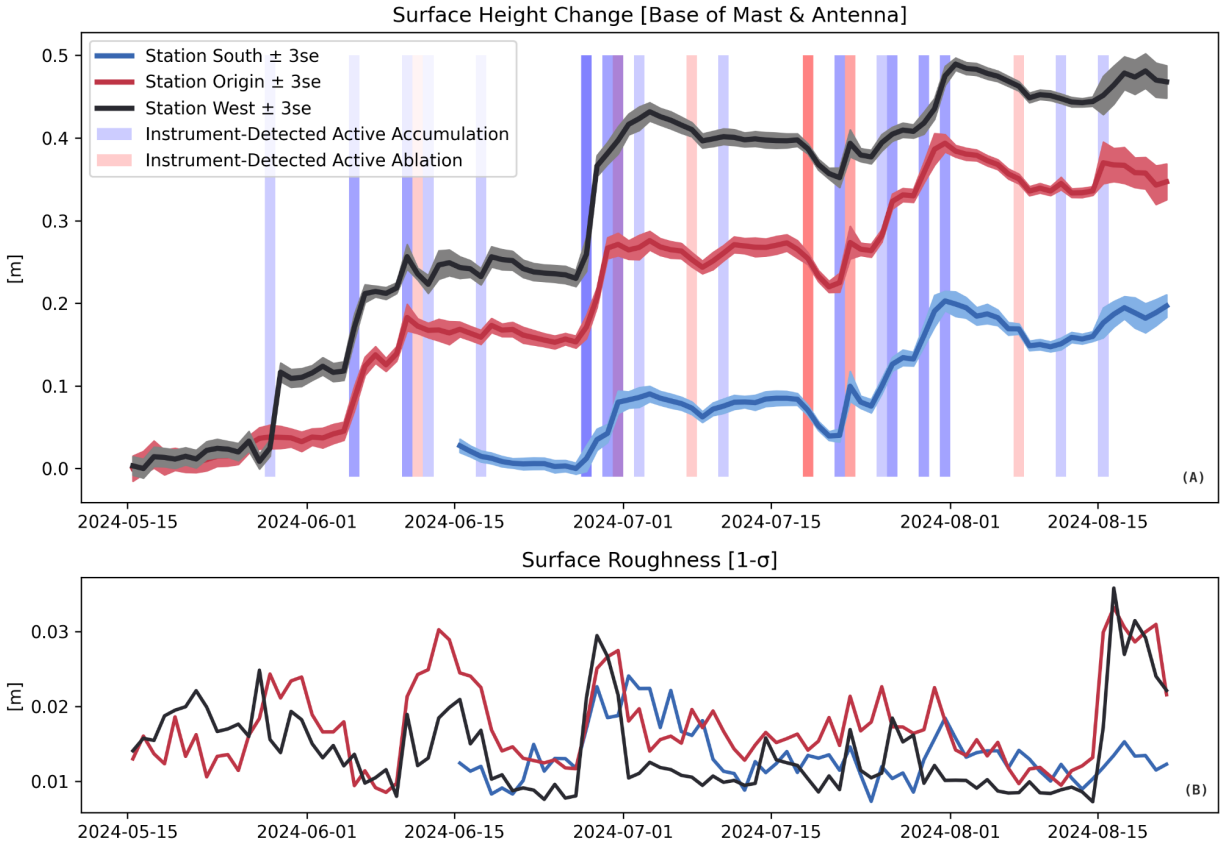
Extended Data Fig. 5 | A comparison of the (a) net shortwave and (b) net longwave components of the radiative budget for only clear sky times between ICECAPS' sensors and the nearby AWS. The differences characterized in the main text are also present here in terms of the smearing of the distribution to large values of **(a)** net shortwave and a general mean bias in the **(b)** longwave.



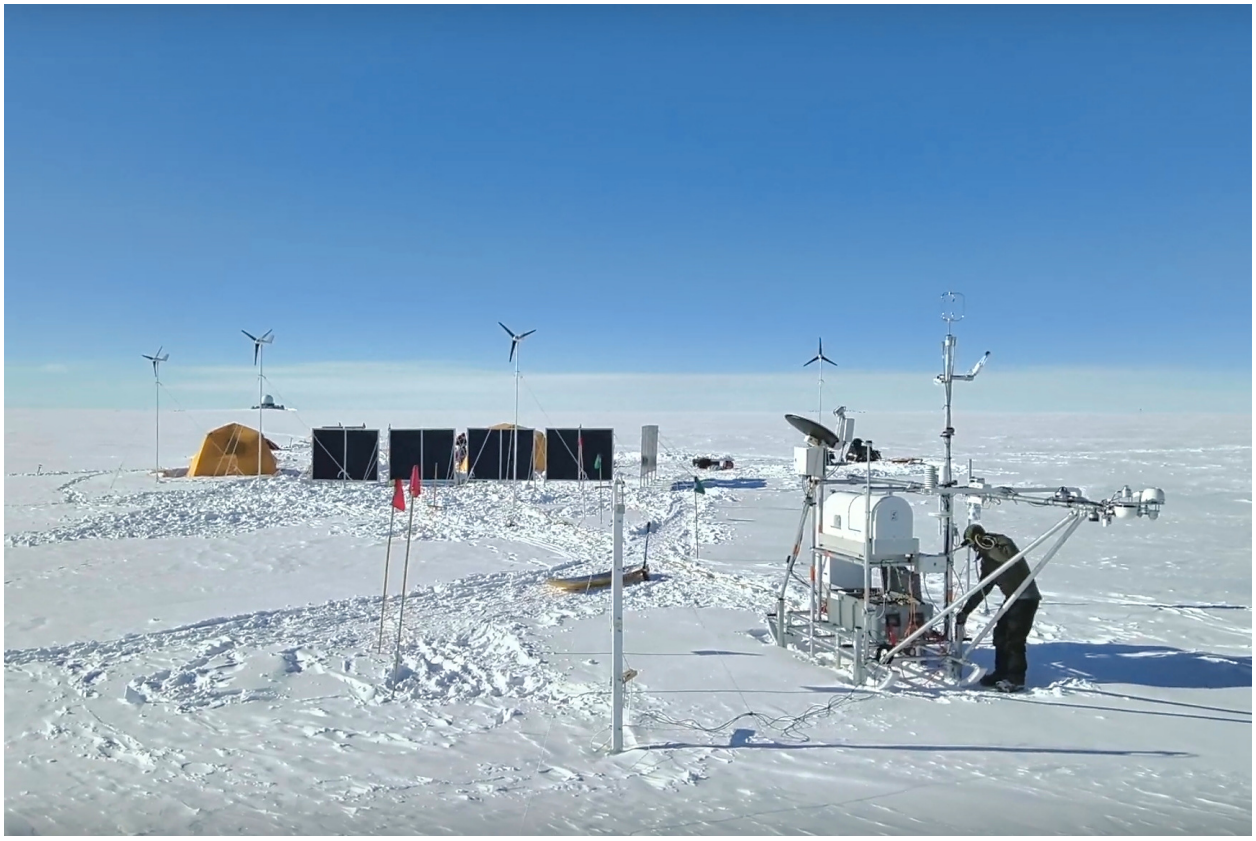
Extended Data Fig. 6 | Outgoing shortwave plotted against incoming shortwave with lines to demarcate albedo regimes for (a) ICECAPS and (b) AWS measurements. The difference in albedo during clear skies at large incoming shortwave manifests here as a larger number of tan points below the 0.8 albedo demarcation.



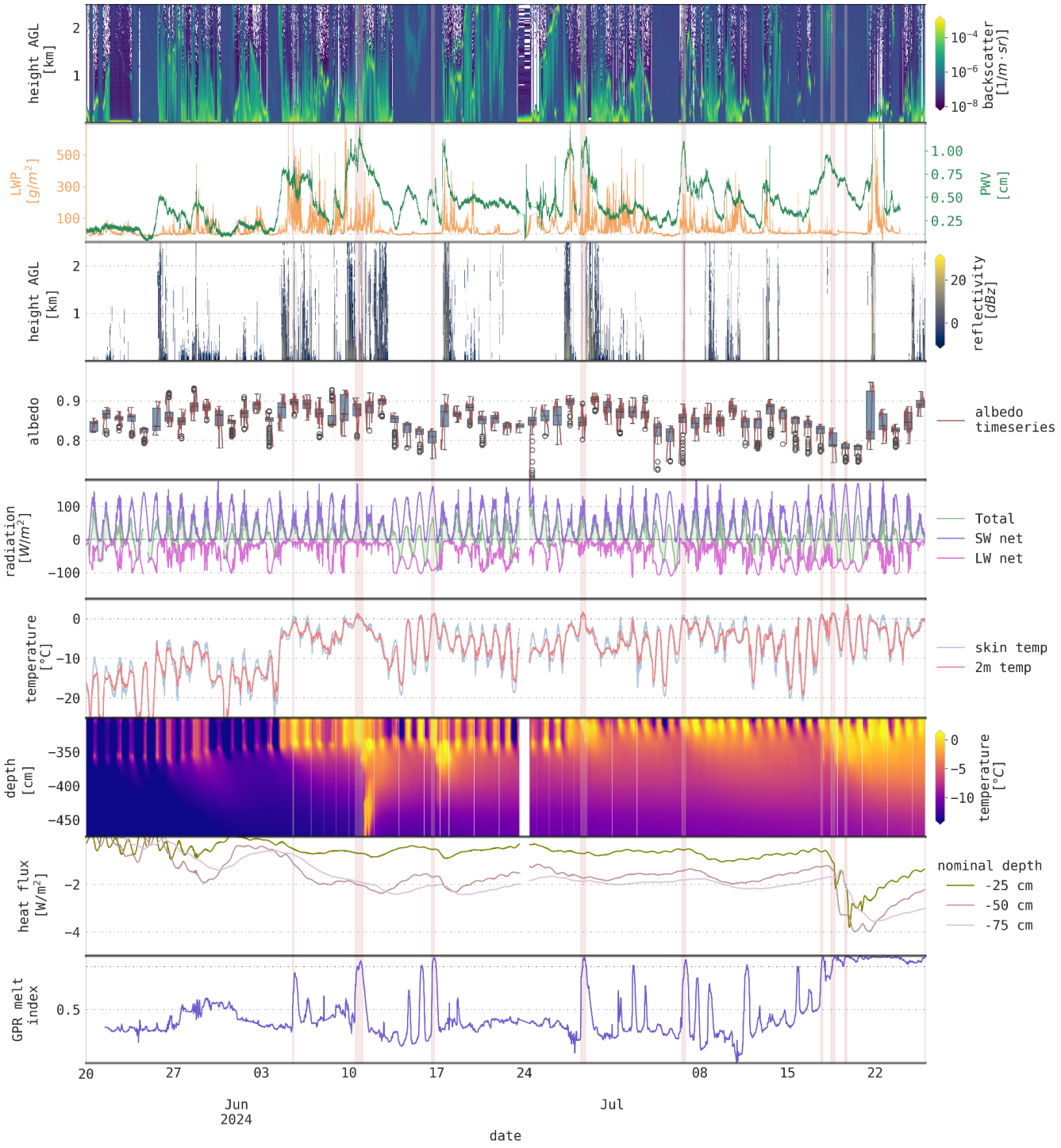
Extended Data Fig. 7 | (a) Albedo plotted against incoming shortwave alongside (b) outgoing shortwave plotted against incoming shortwave down with lines to demarcate albedo regimes for a different AWS measurement site on the K-transect. Plotted for May of 2023, a brief time window when there is fresh snow and little variation in surface characteristics, to illustrate that the critical identified features in the DYE-2 AWS radiation measurements are also present in data from another location on the ice sheet.



Extended Data Fig. 8 | (a) Spatial surface height changes and (b) roughness estimate retrieved from GNSS reflectometry stations. These data provide independent assessment of surface changes corresponding to atmospheric events with a footprint substantially larger than that of the autonomous platform alone.



Extended Data Fig. 9 | A photograph of the ICECAPS autonomous platform (foreground) and the renewable energy power system (background).



1245

1246 **Extended Data Fig. 10 | A complete time series of the ICECAPS data from summer**
1247 **2024,** plotted as in Figs. 2 and 3. Red vertical bands highlight periods of time where
1248 active surface melt was identified using a combination of sensors.